

Manuscript Number: EPSL-D-16-00961R2

Title: Static versus dynamic fracturing in shallow carbonate fault zones

Article Type: Letters

Keywords: in-situ shattering; dynamic loading; earthquakes; quasi-static loading; carbonates; fractures

Corresponding Author: Dr. Michele Fondriest, PhD

Corresponding Author's Institution:

First Author: Michele Fondriest

Order of Authors: Michele Fondriest; Mai-Linh Doan; Frans Aben; Florian Fuisseis; Tomas M Mitchell; Maarten Voorn; Michele Secco; Giulio Di Toro

Abstract: Moderate to large earthquakes often nucleate within and propagate through carbonates in the shallow crust. The occurrence of thick belts of low-strain fault-related breccias is relatively common within carbonate damage zones and was generally interpreted in relation to the quasi-static growth of faults. Here we report the occurrence of hundreds of meters thick belts of intensely fragmented dolostones along a major transpressive fault zone in the Italian Southern Alps. These fault rocks have been shattered in-situ with negligible shear strain accumulation. The conditions of in-situ shattering were investigated by deforming the host dolostones in uniaxial compression both under quasi-static (strain rate $\sim 10^{-5}$ s $^{-1}$) and dynamic (strain rate > 50 s $^{-1}$) loading. Dolostones deformed up to failure under low-strain rate were affected by single to multiple discrete extensional fractures sub-parallel to the loading direction. Dolostones deformed under high-strain rate were shattered above a strain rate threshold of ~ 120 s $^{-1}$ and peak stresses on average larger than the uniaxial compressive strength of the rock, whereas they were split in few fragments or remained macroscopically intact at lower strain rates. Fracture networks were investigated in three dimensions showing that low- and high-strain rate damage patterns (fracture intensity, aperture, orientation) were significantly different, with the latter being similar to that of natural in-situ shattered dolostones (i.e., comparable fragment size distributions). In-situ shattered dolostones were thus interpreted as the result of high energy dynamic fragmentation (dissipated strain energies > 1.8 MJ/m 3) similarly to pulverized rocks in crystalline lithologies. Given their seismic origin, the presence of in-situ shattered dolostones can be used in earthquake hazard studies as evidence of the propagation of seismic ruptures at shallow depths.

1 **Static versus dynamic fracturing in shallow carbonate fault zones**

2 Authors: Michele Fondriest^{1*}, Mai-Linh Doan², Frans Aben², Florian Fousseis³, Tomas M.
3 Mitchell⁴, Maarten Voorn⁵, Michele Secco^{6,7}, Giulio Di Toro^{1,8,9}

4

5 ¹ School of Earth, Atmospheric and Environmental Sciences, University of Manchester, M139PL,
6 Manchester, UK

7 ² ISTerre, Université Grenoble Alpes, CS 40700, GRENOBLE Cedex 9, FR

8 ³ School of Geosciences, University of Edinburgh, EH9 3FE, Edinburgh, UK

9 ⁴ [Rock & Ice Physics Laboratory & UCL Seismolab](#), Department of Earth Sciences, University
10 College London, WC1E 6BT, London, UK

11 ⁵ Department of Geodynamics and Sedimentology, University of Vienna, Althanstrasse 14, 1090
12 Vienna, AUT - now at Baker Hughes.

13 ⁶ Department of Civil, Environmental and Architectural Engineering (ICEA), University of Padova,
14 via Francesco Marzolo 9, Padua, IT

15 ⁷ Inter-departmental Research Center for the Study of Cement Materials and Hydraulic Binders
16 (CIRCe), University of Padua, IT

17 ⁸ Dipartimento di Geoscienze, University of Padova, via G. Gradenigo 6, 35131, Padua, IT

18 ⁹ Istituto Nazionale di Geofisica e Vulcanologia (INGV), via di Vigna Murata 605, 00143, Rome, IT

19

20

21 **Keywords:** in-situ shattering, dynamic loading, earthquakes, quasi-static loading, carbonates,

22 fractures

23

24 **ABSTRACT**

25 Moderate to large earthquakes often nucleate within and propagate through carbonates in the
26 shallow crust. The occurrence of thick belts of low-strain fault-related breccias is relatively
27 common within carbonate damage zones and was generally interpreted in relation to the quasi-
28 static growth of faults. Here we report the occurrence of hundreds of meters thick belts of
29 intensely fragmented dolostones along a major transpressive fault zone in the Italian Southern
30 Alps. These fault rocks have been shattered *in-situ* with negligible shear strain accumulation.
31 The conditions of *in-situ* shattering were investigated by deforming the host dolostones in
32 uniaxial compression both under quasi-static (strain rate $\sim 10^{-5} \text{ s}^{-1}$) and dynamic (strain rate $>$
33 50 s^{-1}) loading. Dolostones deformed up to failure under low-strain rate were affected by single
34 to multiple discrete extensional fractures sub-parallel to the loading direction. Dolostones
35 deformed under high-strain rate were shattered above a strain rate threshold of $\sim 120 \text{ s}^{-1}$ and
36 peak stresses **on average** larger than the uniaxial compressive strength of the rock, whereas
37 they were split in few fragments or remained macroscopically intact at lower strain rates.
38 Fracture networks were investigated in three dimensions showing that low- and high-strain
39 rate damage patterns (fracture intensity, aperture, orientation) were significantly different,
40 with the latter being similar to that of natural *in-situ* shattered dolostones (i.e., comparable
41 fragment size distributions). *In-situ* shattered dolostones were thus interpreted as the result of
42 high energy dynamic fragmentation (dissipated strain energies $> 1.8 \text{ MJ/m}^3$) similarly to
43 pulverized rocks in crystalline lithologies. Given their seismic origin, the presence of *in-situ*

44 shattered dolostones can be used in earthquake hazard studies as evidence of the propagation
45 of seismic ruptures at shallow depths.

46

47 **1. INTRODUCTION**

48 Unstable fracture propagation and fragmentation are fundamental processes
49 dominating brittle deformation of solid materials loaded upon and beyond their elastic limit
50 (e.g., Scholz, 2002). The mechanics of fracturing is strongly controlled by the loading
51 configuration (tensile or compressive) since in tension a single crack can grow unstably (i.e.,
52 accelerating) until sample failure, whereas in compression a population of small cracks
53 propagates stably (i.e., steady growth rate) until stress interaction leads to instability and
54 sample failure (Ashby and Sammis, 1990). Fracture [growth rates can range from stable quasi-](#)
55 [static low velocities to dynamic ones](#) comparable or higher than the Rayleigh wave velocity of
56 the host material (e.g., Freund, 1990).

57 These considerations are particularly relevant when applied to rocks and fault zones in
58 which fractures are widespread. Experimental deformation of both rocks and analogue
59 materials (e.g., polymer composites) investigated the spectrum of propagation rates, from
60 [stable](#) to dynamic, for growing shear and tensile [single](#) fractures nucleated under various
61 loading configurations. As a result two major features, namely high angle tensile fractures and
62 macro- to micro branching were recognized to be exclusively associated to dynamic [fracture](#)
63 [propagation](#) (e.g., Sagy et al., 2001; Griffith et al., 2009; Fineberg et al., 1991, 1999). High angle
64 tensile fractures compare well with off-fault injection veins which are currently considered as
65 clear evidence of earthquake ruptures in the field, especially when filled with pseudotachylites

66 or fluidized fault rocks (Di Toro et al., 2005; Rowe and Griffith, 2015). Conversely this is not the
67 case for branching fractures which can even be induced by quasi-static loading (Sagy et al.,
68 2004). This means that besides investigating the growth velocity of single fractures, it is
69 important to determine the loading conditions (e.g. loading and strain rates) responsible for the
70 production of certain fracture patterns both in experiments and in nature.

71 The characterization of rock damage and the identification of dynamic signatures within
72 fault zones have fundamental implications for earthquake mechanics and in particular for the
73 constraint of energy budgets involved in seismic fracturing (e.g., Shipton et al., 2006; Pittarello
74 et al., 2008). To date rock pulverization (i.e., fragmentation down to the crystal size scale with
75 no shear strain accommodation) is the only large-scale macroscopic feature clearly relatable to
76 dynamic off-fault damage induced during the propagation of earthquake ruptures. Indeed
77 pulverized rocks have been reported in tens to hundreds of meters thick bands along major
78 faults (Dor et al., 2006, Mitchell et al., 2011) and were produced in the laboratory under high
79 strain rate loading conditions (Doan and Gary, 2009; Yuan et al., 2011). Fine-grained pulverized
80 rocks (sensu Brune et al., 2001) seem to be exclusively formed at shallow depth (less than 3 km)
81 within homogeneous stiff protoliths (mainly granitoids) while their occurrence was not
82 frequently reported for heterogeneous sedimentary covers. The latter is the case for
83 carbonates (i.e., limestones and dolostones), which are worldwide distributed lithologies
84 dominating the upper crust of many seismically active regions where moderate to large
85 magnitude earthquakes occur (e.g., 2008 Wenchuan Mw 7.9 and 2009 L'Aquila Mw 6.1
86 earthquakes; Burchfiel et al., 2008; Chiarabba et al., 2009). In particular, the occurrence of thick
87 belts (10-100s m) of low-strain, poorly distorted breccias (average size of rock fragments > 1

88 cm) is common within carbonate fault zones of various kinematics exhumed from a few
89 kilometers (e.g., Billi et al., 2003). These damage patterns were frequently interpreted in
90 relation to the quasi-static growth of fault zones characterized by the sequential formation and
91 activation of joints, pressure solution seams, veins, shear fractures during prolonged polyphasic
92 deformations (e.g., Salvini et al., 1999; Billi et al., 2003; Agosta et al., 2006).

93 Here we investigate the alternative possibility that some of these fragmented rocks in
94 carbonate fault zones may have a coseismic dynamic origin. We report the occurrence of thick
95 belts of *in-situ* shattered dolostones along a major transpressive fault zone in the Italian
96 Southern Alps and test the mechanical behavior of the dolomitic host rocks in compression over
97 a wide range of strain rates ($10^{-6} - 10^2 \text{ s}^{-1}$) to constrain the deformation conditions under which
98 *in-situ* shattering occurs. We used image analysis techniques to discriminate between quasi-
99 static and dynamic fracture patterns and inferred *in-situ* shattering as a dynamic coseismic
100 process. We finally consider the implications of our experimental results for the mechanics of
101 earthquakes and the scaling relationships of fault zones in carbonates.

102

103 **2. IN-SITU SHATTERED DOLOSTONES OF THE FOIANA FAULT ZONE**

104 The Foiana Fault Zone is a ~30 km long major sinistral transpressive fault exhumed from
105 < 2 km depth in the Italian Southern Alps. The fault zone crosscuts Permo-Triassic igneous and
106 sedimentary rocks, the latter including thick sequences of dolostones, with cumulative vertical
107 throw of 0.3-1.8 km (Fig. 1a) (Prosser, 1998). The host rock (Mendola Formation – peritidal
108 member) consists of light-gray sedimentary dolostones with cycles up to 0.6–1 m thick
109 characterized by stromatolitic laminations and planar trails of *fenestrae* (Avanzini et al., 2001;

110 Fondriest et al., 2015). The crystal size is in the range 20-300 μm , with the larger crystals filling
111 diagenetic pores (see Fondriest et al., 2015 for full description). Measured acoustic/elastic
112 properties of the host dolostones are: $V_p = 6.54 \pm 0.46$ km/s, $V_s = 3.64 \pm 0.15$ km/s, dynamic
113 Young modulus= 94.04 ± 9.04 GPa, while total Helium porosity is 1.7 ± 0.8 % (see
114 Supplementary Material).

115 The fault zone is exposed within badland areas and consists of > 300 m thick belts of intensely
116 fractured and fragmented dolostones which have been shattered *in-situ* with negligible shear
117 strain accumulation (Fig. 1b, see Fondriest et al., 2015). This is documented by the preservation
118 of primary sedimentary features (i.e., bedding surfaces, marly dolostone horizons and
119 stromatolitic laminations; see inset in Fig. 1b) even in the most highly fragmented rock bodies.
120 At the outcrop scale dolostones are reduced into fragments ranging from few centimeters
121 down to few millimeters in size separated by joints and extensional micro-fractures. Joints are
122 fault-related and are arranged in different sets (the most pervasive sets are parallel and
123 perpendicular to fault strike; rose diagrams in Fig. 1a) displaying complex cross-cutting/abutting
124 relations (Figs. 1a, b). At the meso- to micro-scale these rocks are affected by a pervasive and
125 non-hierarchical fracture pattern with variable fracture orientations, locally resulting in the
126 development of micro-fragmentation zones (fracture spacing < 1 mm) (Figs. 1c-e). **Fragment**
127 **size distributions (FSD) (also named clast size distributions – CSD) measured in two dimensions**
128 **by manual drawing on thin section scans (area ~ 5 cm²) cover a clast size range of 0.05-7 mm**
129 **with average slopes of 1.2-1.3 in logarithmic plots (Figs. 1e-f) (see Supplementary Materials for**
130 **details). The slopes were computed in the narrower range of 0.4-2 mm where the curves had a**
131 **linear trend (Fig. 7), thus avoiding the external intervals. In fact, the latter are affected by bias**

132 related to the spatial resolution of the images (data truncation) and to the finite size of the
133 analysis domain (data censoring). The clast size distributions determined on fault parallel and
134 fault perpendicular orientations were comparable (Fig.1f).

135

136 3. METHODS

137 To understand the origin of the *in-situ* shattered dolostones of the Foiana Fault Zone
138 low- to high- strain rate uniaxial compression experiments were performed on rock cylinders
139 cored from the Mendola Formation. Low-strain rate ($\sim 10^{-5} \text{ s}^{-1}$) tests were performed with a
140 uniaxial hydraulic test apparatus at the Rock and Ice Physics Laboratory at University College
141 London and a uniaxial hydraulic press at the Geoscience Department rock deformation
142 laboratory in Padova. High-strain rate ($> 50 \text{ s}^{-1}$) tests were conducted with a mini-Split
143 Hopkinson Pressure Bar (SHPB) at the ISTerre laboratory in Grenoble (Aben et al., 2016a).
144 Quasi-static uniaxial tests (N=16) were run both in displacement and stress control mode on 20
145 and 25 mm in diameter rock cylinders with various length/diameter ratios (~ 1 -2.4) (Table 1).
146 Dynamic SHPB tests (N=29) were run on samples with length/diameter ratio ~ 1 to reduce
147 inertia effects (Gama et al., 2004; Zhang and Zhao, 2014) and diameters of 10, 15 and 20 mm to
148 explore a wide range of peak stresses and strain rates (Table 1). Applied strain (i.e., loading
149 duration) was controlled by changing the length of the steel striker bar while striker impact
150 velocity was kept fixed around 5 m/s. Cardboard pulse shapers were used to guarantee stress
151 equilibrium conditions during the tests. Further details on the different apparatuses are
152 summarized in Supplementary Material.

153 Some of the samples were wrapped with a heat-shrinkable plastic jacket to be
154 recovered after the experiments (both quasi-static and dynamic loading tests) and analyze the
155 produced fracture pattern. Deformed samples were impregnated with epoxy and petrographic
156 thin sections cut both perpendicular and approximately parallel to the loading direction were
157 prepared for microstructural observations [optical microscopy (OM) and scanning electron
158 microscopy (SEM)]. Three dimensional fracture patterns were described through image analysis
159 techniques (software: FIJI, CTAn) applied to X-ray scan datasets acquired at different spatial
160 resolutions ($8 \times 8 \times 8 \mu\text{m}^3$ and $23 \times 23 \times 23 \mu\text{m}^3$ per voxel), while fragment size distribution (FSD)
161 was determined in two dimensions both for natural and experimental shattered rocks (see
162 Supplementary Material for details).

163

164 **4. RESULTS**

165 *4.1. MECHANICAL DATA AND DAMAGE STATES*

166 Quasi-static uniaxial compression tests were performed on both jacketed and
167 unjacketed samples with varying length to diameter ratio at strain rates of $6.7 \times 10^{-6} \text{ s}^{-1}$ and
168 $6.7 \times 10^{-5} \text{ s}^{-1}$. Measured uniaxial strengths (UCS) and static Young moduli (average values: $227.3 \pm$
169 45 MPa and $64.1 \pm 18 \text{ GPa}$ respectively, see Supplementary Material) were relatively scattered
170 and did not show any correlation with either strain rate or sample geometry (Fig. 2a). The
171 observed variability was likely a consequence of the mechanical heterogeneity of the tested
172 rock. Samples loaded up to failure accumulated permanent axial strains of 0.2-0.7% while
173 elastic strain energy ($E_{diss-\sigma_{MAX}}$ in Table 1, calculated as the area below the “axial stress vs. axial
174 strain” curve) dissipated up to the peak stress was $0.4\text{-}1 \text{ MJ/m}^3$. The common failure mode was

175 longitudinal “sub-axial” splitting (*sensu* Holzhausen and Johnson, 1979) with fractures oriented
176 parallel or at small angle ($<10^\circ$) to the loading direction and cutting through the entire sample.
177 Many of these fractures were concentrated in the outer portion of the sample, where radial
178 expansion is expected to be higher, and had a curvilinear trace in plain view (exfoliation
179 extensional fractures) (Figs. 2b, c). Instead, the central portion of the sample consisted of a
180 continuous "pillar" affected by short (<5 mm trace length) closed shear fractures and staircase
181 arrays of oblique fractures and sub-axial wing cracks (Figs. 2b, c). In some cases the
182 development of a through going Andersonian-oriented leading shear fracture (i.e., sample
183 faulting) was observed (inset in Fig. 2a).

184 Dynamic SHPB tests performed on both jacketed and unjacketed samples spanned peak
185 stresses of 60-360 MPa, axial strains of 0.3-3% and peak strain rates of $140-450\text{ s}^{-1}$ (Table 1,
186 Figs. 3-4). The stress, strain and strain rate histories of the dynamically loaded samples highlight
187 the applied peak stress and the critical strain rate (ϵ'_c in Table 1) as primary factors in
188 controlling the mechanical behavior and the ultimate damage state of the samples. As
189 previously observed by Aben et al. (2016a) the critical strain rate ϵ'_c represents the plateau or
190 inflection point value of the strain rate vs. time curve and roughly matches in time with the
191 applied peak stress (Figs. 3a,b). When recovered after loading the samples were (i)
192 macroscopically intact (Fig. 3a), (ii) split in few pieces (Fig. 3b), or (iii) intensely fragmented (Fig.
193 3c). Samples loaded at critical strain rates of $\sim 20\text{ s}^{-1}$ and peak stresses of 100-150 MPa (below
194 the average UCS limit, Figs. 4a, b) showed a quasi-elastic stress-strain behavior (residual strains
195 $\sim 0.2\%$, Figs. 3a, d) and were macroscopically intact or split if they contained preexisting
196 heterogeneities (e.g., sub-axial veins, Fig. 3a). Samples loaded at critical strain rates $\sim 50\text{ s}^{-1}$ and

197 peak stresses ≤ 200 MPa (around the average UCS limit, Figs. 4a, b) accumulated residual strains
198 of 0.4-0.6% (Figs. 3b, d) and were split or macroscopically intact (Fig.3b). Samples loaded at
199 critical strain rates $> 120 \text{ s}^{-1}$ and peak stresses of ≥ 200 MPa (around and over the average UCS
200 limit, Figs. 4a, b) accumulated residual strains $> 2\%$ (Figs. 3c, d) and were typically intensely
201 fragmented (Fig. 3c). In this case the strain rate at which fragmentation occurred was a relative
202 minimum in the strain rate vs. time curve, preceding a second strain rate peak occurring during
203 sample unloading (Aben et al., 2016a) (Fig.3c). Dissipated strain energy during fragmentation
204 was in the range 1.5-2.8 MJ/m³ (E_{diss} in Table 1), almost 30% of the kinetic energy transferred by
205 the striker impact to the steel bar (E_{kin} in Table 1, calculated as $E_{kin} = 0.5 \times m \times v^2$, where m is the
206 striker mass and v the striker impact velocity; Fig. 4c). These samples were reduced into a non-
207 cohesive material with angular rock fragments mostly of few millimeters in size (Fig. 3c).
208 Looking at *in-situ* microstructures (X-ray tomography and microscopy on thin sections), the
209 fragments were elongated in the loading direction and delimited by subparallel extensional
210 fractures crosscut by a few orthogonal ones (Figs. 5a, b). Diffuse tensile microfracturing
211 exploiting both cleavage planes and grain boundaries occurred along the main fractures and at
212 the side where the stress wave entered the sample (Figs. 5c, d). Such microstructures, coupled
213 with the general absence of shear strain, are very similar in natural *in-situ* shattered dolostones
214 (compare Figs. 5a, d with Figs. 1c-e).

215 4.2. FRACTURE PATTERN ANALYSIS

216 The three-dimensional fracture patterns of quasi-statically and dynamically deformed
217 samples were quantified and compared by using image analysis applied to X-ray computed
218 tomography datasets (for details see Supplementary Material) (Figs. 6a-c). To extract the

219 fracture network from the tomographic images we used the approach implemented by Voorn
220 et al. (2013) (multiscale Hessian fracture filter – MSHFF) for the software FIJI (Schindelin et al.,
221 2012), which was optimized for the enhancement and segmentation of narrow planar features
222 such as fractures (see Supplementary Material). Further properties of the fracture network such
223 as fracture intensity, bulk fracture orientation and aperture were determined after Voorn et al.
224 (2015) using both FIJI and CTAn software (for details see Supplementary Material). The fracture
225 skeletons were analyzed in two dimensions on slices oriented orthogonal to the loading
226 direction.

227 Volumetric fracture intensity values (total fracture surface/sample volume) were
228 significantly higher for dynamically shattered samples ($\sim 4.0 \text{ mm}^{-1}$) compared to quasi-statically
229 fractured ones ($\sim 1.4 \text{ mm}^{-1}$) (Fig. 6b). Bulk fracture aperture followed a unimodal distribution
230 (modal value $\sim 0.03 \text{ mm}$ for samples S4 and S26, Fig. 6c) in shattered samples while it was
231 characterized by a polymodal distribution (modal values $> 0.1 \text{ mm}$ for sample U4, Fig. 6c) in
232 quasi-statically fractured samples. In both cases fractures were oriented almost parallel to the
233 loading direction (Fig. 6b). In terms of strike fractures generated under dynamic loading were
234 quite scattered or arranged in a orthorhombic geometry (“low hierarchy” fracture pattern),
235 while fractures produced under quasi-static loading were clustered around the orientation of
236 few leading fractures (“high hierarchy” fracture pattern) (Figs. 6a, b). Overall the fracture
237 patterns produced by dynamic loading were characterized by a much higher number of fracture
238 branches and intersections compared to the quasi-static ones (Fig. 6d).

239 *4.3. FRAGMENT SIZE DISTRIBUTIONS OF THE SHATTERED DOLOSTONES*

240 Fragment size distributions (FSD) of experimental shattered dolostones were
241 determined in two dimensions by manual drawing on X-ray tomographic images over an area of
242 $\sim 0.8 \text{ cm}^2$ which was constrained by the dimensions of the experimental samples (for details
243 see Supplementary Material). To allow a comparison, the FSDs of natural shattered dolostones
244 (see Fig.1f) were recalculated on the same smaller analysis domains (area $\sim 0.8 \text{ cm}^2$) (Fig.7). The
245 resulting FSDs of both natural and experimental shattered dolostones were comparable in the
246 size range 0.01-4 mm with an average slope of 0.73 ± 0.14 in logarithmic plots (Fig.7). The slopes
247 were computed in the narrower range of 0.1-1 mm where the curves had a linear trend (Fig.7),
248 thus avoiding the external intervals which are affected by bias related to the spatial resolution
249 of the images (data truncation) and to the finite size of the analysis domain (data censoring).
250 Recalculated slopes (D) of natural shattered dolostones are smaller (~ 0.7 on average; Fig.7)
251 than the ones determined on larger analysis domains (~ 1.2 on average; Fig.1f). The different
252 slopes in the fragment distributions plots are certainly due to the undersampling effects
253 associated to the reduction of the analysed sampled area. However, the diverse slopes might
254 also suggest that the FSDs of these rocks are neither spatial heterogeneous nor self-similar. To
255 investigate this hypothesis it would be necessary to determine the fragment size distributions
256 over a much larger size range (i.e. three to four orders of magnitude).

257 **5. DISCUSSION AND CONCLUSIONS**

258 *5.1. ENERGY SINKS AND DAMAGE*

259 Experimental results indicate that intensely fragmented *in-situ* shattered dolostones
260 were produced in compression when the applied critical strain rate was $> 120 \text{ s}^{-1}$ and the peak
261 stress was on average larger than the uniaxial compressive strength of the rock (227.3 ± 45

262 MPa) (Figs. 4a-c). In particular, when we considered the strain energy dissipated in the sample
263 up to the peak stress ($E_{diss-\sigma MAX}$ in Table 1), the occurrence of an energy threshold of ~ 1.8
264 MJ/m³, above which *in-situ* shattering start to develop, was evident (Fig.8). Interestingly this
265 energy threshold was larger than the total energy dissipated in the pulverization of crystalline
266 rocks such as quartz-monzonite (~ 1.5 MJ/m³; Aben et al., 2016a) and calcitic marble (~ 1.1
267 MJ/m³; Doan and Billi, 2011). Estimates of surface fracture energies for the shattered samples
268 (E_S in Table 1) were 40-80% of dissipated strain energy (E_{diss} in Table 1, see Supplementary
269 Material). The dynamically fragmented samples had distinctive characteristics compared to
270 quasi-statically fractured ones: (i) higher fracture intensity, (ii) narrower fractures, (iii) low-
271 hierarchy and high-complexity of the fracture pattern (Figs. 6a-d). All these characteristics are
272 consistent with high strain rate loading during which the energy supply to the sample is too fast
273 to be dissipated by only few fractures: this results in intense fragmentation of the rock (Grady
274 and Kipp, 1989; Bhat et al., 2012; Doan and d'Hour, 2012, Aben et al, 2016b). On the other
275 hand quasi-statically loaded samples displayed typical low-rate propagation features such as
276 subaxial wing cracks growing at the tips of inclined fractures (e.g., Ashby and Sammis, 1990).
277 Instead, the relatively abundance of curvilinear fractures in the outer portion of the samples
278 was due to non-uniform stress distribution and lack of confinement during the tests (Peng and
279 Johnson, 1972), and has to be considered as an artifact when compared with natural fault
280 rocks. This was not the case for dynamically loaded samples, which were instead affected by
281 radial fractures due to the occurrence of dynamic confinement (radial confinement up to ~ 0.5
282 MPa, see Supplementary Material) at high loading rates, when the effect of material inertia
283 becomes significant (Doan and Gary, 2009; Chen, 2011).

284 5.2. IN-SITU SHATTERING: NATURE VS. LAB

285 *In-situ* shattered dolostones were exclusively produced at high dynamic loading rates in
286 the laboratory. The deformation conditions determined for shattering in dolostones (critical
287 strain rate $> 120 \text{ s}^{-1}$, axial strain $> 2\%$, Fig. 4) were comparable to those associated to
288 pulverization of homogeneous crystalline rocks (i.e., granite, quartz-monzonite, calcitic marble;
289 Doan and Gary, 2009; Yuan et al., 2011, Doan and Billi, 2011; Aben et al., 2016a) and considered
290 to be transiently achieved in the fault wall rocks during the propagation of an earthquake
291 rupture (e.g., Ben-Zion and Shi, 2005; Reches and Dewers, 2005). Moreover, in contrast to the
292 quasi-statically deformed samples, experimentally shattered dolostones showed striking
293 similarities with the natural ones of the Foiana Fault Zone: (i) two dimensional FSDs determined
294 at the scale of the experimental samples (area $\sim 0.8 \text{ cm}^2$) were comparable (average slope =
295 0.73 ± 0.14 , size range = 0.01-4 mm) (Figs. 7), (ii) rock fragments were frequently exploded with
296 no evidence of shear strain, (iii) pervasive extensional fracturing locally occurred down to the
297 micrometer scale (microfragmentation domains) (Figs. 1c-e and Figs. 5a-d). All these
298 observations suggest that also natural *in-situ* shattered dolostones had a dynamic origin
299 potentially related to multiple off-fault coseismic stress-wave loadings (Fondriest et al., 2015).

300 5.3 SHATTERED DOLOSTONES AND HYDRAULIC DILATION BRECCIAS

301 The shattered dolostones of the Foiana Fault Zone are characterized by a well-fitted
302 jigsaw puzzle texture which in most of the cases is comparable to that of the *crackle breccias*
303 defined by Woodcock and Mort (2008) in their “non-genetic” fault breccias classification (more
304 than 75% of sample area covered by clasts $> 2 \text{ mm}$ in size). This type of fault breccia was
305 originally described in the dolomitic host rocks of the Dent Fault (northwest England) and

306 characterized by extensive infill of the fracture network by hydrothermal carbonate cement
307 (Tarasewicz et al., 2005; Woodcock et al., 2006). In a similar way many *crackle* and *shatter*
308 breccias described in the mining literature as fault-related were associated to hydraulic
309 implosion mechanisms and frequently cemented by the deposition of hydrothermal minerals
310 (e.g., Phillips, 1972; Mitcham, 1974; Sibson, 1986). According to Sibson (1986) implosive
311 brecciation is a dynamic coseismic process generated by a sudden collapse of the wall rock at
312 dilational fault jogs (mainly during rupture arrest) coupled with the generation of strong pore
313 fluid pressure gradients. Compared to implosion hydraulic breccias, the shattered dolostones of
314 the Foiana Fault Zone (i) were observed in different fault zone sections (straight fault segments
315 and restraining bends; Fig. 1a) and, (ii) did not show presence of veins or cement filling the
316 fracture network (see Fondriest et al., 2015 for details). Basing on the experimental results
317 presented in this study (all the experiments were performed in “dry”- room humidity
318 conditions, see section 3) *in-situ* shattered dolostones of the Foiana Fault Zone are the result of
319 off-fault coseismic damage due to the propagation of multiple earthquake ruptures in a relative
320 fluid-poor environment. This hypothesis might be furtherly reinforced by the occurrence of
321 other structural features such as highly localized mirror-like fault surfaces lined by thin
322 ultracataclastic layers, sharply truncating the shattered dolostones and previously interpreted as
323 evidence of extreme coseismic shear strain localization based on field, microstructural and
324 experimental observations (see for more details Fondriest et al., 2013, 2015).

325 5.4. IMPLICATIONS FOR SCALING RELATIONS IN FAULT ZONES

326 The experimental observations presented [here](#) open the possibility to reinterpret the
327 origin of low-strain breccias (10-100s m thick) frequently associated with fault zones in

328 carbonates and classically interpreted in relation to the “slow” quasi-static growth of faults (i.e.,
329 nucleation and interaction of various generations of joints, pressure solution seams and shear
330 fractures; e.g., Salvini et al., 1999; Billi et al., 2003; Agosta et al., 2006). Many of these breccias,
331 especially within stiff dolomitic protoliths, might instead be produced by dynamic shattering
332 during the propagation of earthquake ruptures and then be more efficiently affected by
333 dissolution-precipitation and mass transfer processes during the post- or inter-seismic periods
334 (e.g., Gratier et al. 2014). Following this line of thought most of the volume of these fault zones
335 would be generated during earthquakes as it is also suggested by aftershocks spatial
336 distributions along active seismogenic faults (e.g., Valoroso et al., 2013). Moreover faults
337 associated with *in-situ* shattered fault rocks are frequently characterized by thickness vs.
338 displacement (t/d) ratios which are significantly higher (i.e., $t/d \sim 1$) compared to the classical
339 scaling relations estimated for relatively “simpler” fault zones (i.e., characterized by discrete
340 fault surfaces and well described by the “*damage zone-fault core*” model of Caine et al., 2010)
341 according to purely geometric quasi-static growth models ($t/d \sim 0.1$; e.g., Childs et al., 2009).
342 This is particularly evident within near-tip fault sections, as in the case of the southern sector of
343 the Foiana Fault Zone, where cumulative displacement tends to be low and the effects of slip
344 accumulation by stable sliding are likely to be minimized (Fig. 9). Therefore the occurrence of
345 high thickness vs. displacement ratios, coupled with the presence of *in-situ* shattered fault
346 rocks, can potentially be used to assess (i) the propagation of earthquake ruptures at shallow
347 depth along carbonate fault zones, and (ii) the hazard related to seismogenic sources with
348 incomplete earthquake catalogs. As a consequence the accurate mapping of the distribution of
349 *in-situ* shattered fault rocks along seismogenic fault zones and the precise quantification of

350 their fracture intensity represent the base for future robust evaluations of the actual
351 contribution of surface fracture energy in the earthquake energy balance at shallow depth (i.e.,
352 < 3 km).

353

354 **Acknowledgments**

355 MF performed all the experiments in collaboration with MLD and FA (SHPB tests) and TMM
356 (uniaxial compression tests), the microstructural analyses in collaboration with FF and MS (X-
357 ray microtomography) and MV (fracture pattern analysis), and wrote the first version of the
358 manuscript. All the authors contributed to revise the final version of the manuscript. [The](#)
359 [detailed comments of Shalev Siman-Tov and Tom Blenkinsop greatly improved the quality of](#)
360 [the manuscript](#). MF thanks Marco Avanzini, who introduced him to the outcrops of the Foiana
361 Fault Zone; Leonardo Tauro, Elena Masiero, Joséphine Gervin, Matteo Parisatto, Mark Jefferd,
362 Lorenzo Raccagni, Bruno Ciervo, Stefano Castelli and Luca Peruzzo for technical and
363 microanalytical support. MF and GDT acknowledge the European Research Consolidator Grant
364 (No. 614705) NOFEAR. MS thanks Fondazione Cassa di Risparmio di Padova e Rovigo (CaRiPaRo)
365 for financial support. [TMM acknowledges support from NERC grant ref NE/M004716/1.](#)

366

367 **Reference list**

368 **Aben, F.M.**, Doan, M.-L., Mitchell, T.M., Toussaint, R., Reuschlé, T., Fondriest, M., Gratier, J.-P.,
369 Renard, F., 2016a. Dynamic fracturing by successive coseismic loadings leads to pulverization in
370 active fault zones, *J. Geophys. Res. Solid Earth*, 121, 2338–2360, doi:10.1002/2015JB012542.

371 **Aben, F.M.**, Doan M.-L., Gratier, J.-P., Renard, F., 2016b. Coseismic damage generation and
372 pulverization in fault zones: insights from dynamic Split-Hopkinson Pressure Bar experiments.
373 In: "Evolution of Fault Zone Properties and Dynamic Processes during Seismic Rupture", edited
374 by M.Y. Thomas, H.S. Bhat, T.M. Mitchell. (in press)

375 **Agosta, F.**, Aydin, A., 2006. Architecture and deformation mechanism of a basin-
376 bounding normal fault in Mesozoic platform carbonates, central Italy. *J. Struct. Geol.* 28
377 (8),1445–1467.

378 **Ahsby, M.F.** and Sammis, C. G., 1990. The damage mechanics of brittle solids in compression,
379 *Pure and Applied Geophysics*, 133, 489-521.

380 **Avanzini, M.**, Bargossi, G.M., Castiglioni, G.B., Dalmeri, G., Eccel, E., Mancabelli, A. , Morelli, C.,
381 Neri, C., Picotti, V., Prosser, G., Sartori, G., Zambotti, G., 2001. Carta Geologica della Provincia
382 di Trento, tav. 26 III Fondo (a scala 1:25.000) con Note illustrative, 159 pp., Provincia Autonoma
383 di Trento, Servizio Geologico.

384 **Ben-Zion, Y.** and Shi, Z., 2005. Dynamic rupture on a material interface with spontaneous
385 generation of plastic strain in the bulk, *Earth and Planetary Science Letters*, 236, 486-496.

386 **Bhat, H.S.**, Rosakis, A.J., Sammis, C. G., 2012. A micromechanics based constitutive model for
387 brittle failure at high strain rates, *Journal of Applied Mechanics*, doi:10.1115/1.4005897.

388 **Billi, A.**, Salvini, F., Storti, F., 2003. The damage zone-fault core transition in carbonate rocks:
389 implications for fault growth, structure and permeability. *J. Struct. Geol.* 25 (11), 1779–1794.

390 **Brune, J.**, 2001. Fault normal dynamic loading and unloading: an explanation for non-gouge
391 rock powder and lack of fault-parallel shear bands along the San Andreas Fault. *EOS Trans. Am.*
392 *Geophys. Union* 82, 47

393 **Burchfiel, B.C.**, Royden, L.H., Van der Hilst, R.D., Hager, B.H., Chen, Z., King, R., Li, C., Lu, Y.,
394 Kirby, E., 2008. A geological and geophysical context for the Wenchuan earthquake of 12 May
395 2008, Sichuan, People's Republic of China, *GSA today*, 18, 5.

396 **Chiarabba, C.** et al., 2009. The 2009 L'Aquila (central Italy) M_w 6.3 earthquake: main shock and
397 aftershocks. *Geophysical Research Letters*, <http://dx.doi.org/10.1029/2009GL039627>.

398 **Chen, W.W.** and Song, B., 2011. Split Hopkinson (Kolsky) Bar - Design, Testing and Applications,
399 Mechanical Engineering Series, Springer.

400 **Childs, C.**, Manzocchi, T., Walsh, J.J., Bonson, C.G., Nicol, A., Schöpfer, M.P.J., 2009. A geometric
401 model of fault zone and fault rock thickness variations. *Journal of Structural Geology* 31,
402 117e127.

403 **Di Toro G.**, Nielsen, S., Pennacchioni, G., 2005. Earthquake rupture dynamics frozen in exhumed
404 ancient faults. *Nature*, 436, 1009-1012.

405 **Doan, M.-L.**, Billi, A., 2011. High strain rate damage of Carrara marble. *Geophys. Res. Lett.* 38
406 (38), L19302. <http://dx.doi.org/10.1029/2011GL049169>.

407 **Doan, M.-L.** and D'Hour, V., 2012. Effect of initial damage on rock pulverization along faults, *J.*
408 *Struct. Geol.*, 45, 113–124, doi:10.1016/j.jsg.2012.05.006.

409 **Doan, M.-L.** and Gary, G., 2009. Rock pulverisation at high strain rate near the San Andreas
410 Fault. *Nat. Geosci.* 2, 709–712.

411 **Dor, O.**, Ben-Zion, Y., Rockwell, T.K., Brune, J., 2006b. Pulverized rocks in the Mojave section of
412 the San Andreas fault zone. *Earth Planet. Sci. Lett.* 245, 642–654.

413 **Fineberg, J.**, Gross, S., Marder, M., and H. Swinney, 1992. Instability in the propagation of fast
414 cracks, *Physical Reviews*, B45, 5146-5154.

415 **Fineberg, J.**, and Marder, M., 1999. Instability in Dynamic Fracture, *Physics Reports*, 313, 1-108.

416 **Fondriest, M.**, Smith, S.A.F., Candela, T., Nielsen, S.B., Mair, K., Di Toro, G., 2013. Mirror-like
417 faults and power dissipation during earthquakes, *Geology*, 41, 1175-1178.

418 **Fondriest, M.**, Aretusini, S., Di Toro, G., Smith, S.A.F., 2015. Fracturing and rock pulverization
419 along an exhumed seismogenic fault zone in dolostones: The Foiana Fault Zone (Southern Alps,
420 Italy), *Tectonophysics*, 654, 56-74.

421 **Freund, L.B.** (1990), *Dynamic Fracture Mechanics*, Cambridge Univ. Press, Cambridge.

422 **Gama, B.A.**, Lopatnikov, S.L., Gillespie, W.J., 2004. Hopkinson bar experimental technique: A
423 critical review, *Appl. Mech. Rev.*, 57(4), 223, doi:10.1115/1.1704626.

424 **Grady, D.E.**, and Kipp, M.E., 1987. Dynamic rock fragmentation, in *Fracture Mechanics of Rock*,
425 Atkinson B. K. ed., Academic Press Geology Series, London.

426 **Gratier, J.-P.**, Renard, F., Vial, B., 2014. Postseismic pressure solution creep: Evidence and
427 time-dependent change from dynamic indenting experiments, *Journal of Geophysical Research*,
428 119, 2764-2779.

429 **Griffith, W.A.**, Rosakis, A., Pollard, D.D., Ko, C.W., 2009. Dynamic rupture experiments elucidate
430 tensile crack development during propagating earthquake ruptures, *Geology*, 37, 795-798.

431 **Holzhausen, G.R.**, and Johnson, A.M., 1979. Analyses of longitudinal splitting of uniaxially
432 compressed rock cylinders, *International Journal of Rock Mechanics and Mining Sciences &*
433 *Geomechanics Abstracts*, 16, 163-177.

434 **Mitcham, T.W.**, 1974. Origin of breccia pipes, *Econ. Geol.*, 69, 412-413.

435 **Mitchell, T.M.**, Ben-Zion, Y., Shimamoto, T., 2011. Pulverized fault rocks and damage
436 asymmetry along the Arima Takatsuki Tectonic Line, Japan, *Earth Planet. Sci. Lett.* 308, 284–297.

437 **Peng, S.**, and Johnson, A.M., 1972. Crack growth and faulting in cylindrical specimens of
438 Chelmsford granite, *International Journal of Rock Mechanics and Mining Sciences &*
439 *Geomechanics Abstracts*, doi:10.1016/0148 9062(72)90050-2.

440 **Phillips, W.J.**, 1972. [Hydraulic fracturing and mineralization. *J. Geol. Soc. Lond.*, 128, 337-359.](#)

441 **Pittarello, L.**, Di Toro, G., Bizzarri, A., Pennacchioni, G., Hadizadeh, J., Cocco, M., 2008. Energy
442 partitioning during seismic slip in pseudotachylyte-bearing faults (Gole Larghe Fault, Adamello,
443 Italy), *Earth and Planetary Science Letters*, 269, 131-139.

444 **Prosser, G.**, 1998. Strike-slip movements and thrusting along a transpressive fault zone: the
445 North Giudicarie line (Insubric line, northern Italy), *Tectonics*, 17, 921–937.

446 **Reches, Z.**, Dewers, T.A., 2005. [Gouge formation by dynamic pulverization during earthquake
447 rupture, *Earth and Planetary Science Letters*, 235, 361-374.](#)

448 **Rowe, C.D.**, and Griffith, W.A., 2015. Do faults preserve a record of seismic slip: A second
449 opinion, *J. Struct. Geol.*, 78, doi:10.1016/j.jsg.2015.06.006.

450 **Sagy, A.**, Reches, Z., Roman, I., 2001. Dynamic fracturing: field and experimental observations,
451 *J. Struct. Geol.*, 23, 1223-1239.

452 **Sagy, A.**, Fineberg, J., Reches, Z., 2004. [Shatter cones: Branched, rapid fractures formed by
453 shock impact, *J. Geophys. Res. B Solid Earth*, 109\(10\), 1–20, doi:10.1029/2004JB003016.](#)

454 **Salvini, F.**, Billi, A., Wise, D.U., 1999. Strike-slip fault-propagation cleavage in carbonate rocks:
455 the Mattinata Fault Zone, Southern Apennines, Italy, *J. Struct. Geol.*, 21, 1731-1749.

456 **Schindelin, J.**, Arganda Carreras, I., Frise, E., Kaynig, V., Longair, M., Pietzsch, T., Preibisch, S.,
457 Rueden, C., Saalfeld, S., Schmid, B., Tinevez, J.Y., White, D.J., Hartenstein, V., Eliceiri, K.,

458 Tomancak, P., Cardona, A., 2012. Fiji:an open-source platform for biological-image analysis.
459 Nat. Methods 9(7), 676–682, <http://dx.doi.org/10.1038/nmeth.2019..>

460 **Scholz, C.H.**, 2002. *The Mechanics of Earthquakes and Faulting*. Cambridge University Press,
461 Cambridge.

462 **Shipton, Z.K.**, Evans, J.P., Abercrombie, R.E., Brodsky, E.E., 2006. The missing sinks: Slip
463 localization in faults, damage zones, and the seismic energy budget. In “Earthquakes: radiated
464 energy and the physics of faulting”, American Geophysical Union monograph, 217-222.

465 **Sibson, R.H.**, 1986. Brecciation processes in fault zones: inferences from earthquake rupturing,
466 *Pure Appl. Geophys.*, 124, 159-175.

467 **Tarasewicz, J.P.T.**, Woodcock, N.H., Dickson, J.A.D., 2005. Carbonate dilation breccias:
468 examples from the damage zone to the Dent Fault, northwest England, *Geol. Soc. Am. Bull.*,
469 117, 736-745.

470 **Valoroso, L.**, Chiaraluce, L., Piccinini, D., Di Stefano, R., Schaff, D., Waldhauser, F., 2013.
471 Radiography of a normal fault system by 64,000 high-precision earthquake locations: the 2009
472 L'Aquila (central Italy) case study. *J. Geophys. Res. Solid Earth*.
473 <http://dx.doi.org/10.1002/jgrb.50130>.

474 **Voorn, M.**, Exner, U., Rath, A., 2013. Multiscale Hessian fracture filtering for the enhancement
475 and segmentation of narrow fractures in 3D image data, *Comput. Geosci.*, 57,44–53.

476 **Voorn, M.**, Exner, U., Barnhoorn, A., Baud, B., Reuschlé, T., 2015. Porosity, permeability and 3D
477 fracture network characterisation of dolomite reservoir rock samples, *Journal of Petroleum*
478 *Science and Engineering*, 127, 270-285.

479 **Woodcock, N.H.**, Omma, J.E., Dickson, J.A.D., 2006. Chaotic breccia along the Dent Fault, NW
480 England: implosion or collapse of a fault void?, *J. Geol. Soc. Lond.*, 163, 431-446.

481 **Woodcock, N.H.**, Mort, K., 2008. Classification of fault breccias and related fault rocks, *Geol.*
482 *Mag.*, 145, 435-440.

483 **Yuan, F.**, Prakash, V., Tullis, T., 2011. Origin of pulverized rocks during earthquake fault rupture.
484 *J. Geophys. Res.* 116, B06309. <http://dx.doi.org/10.1029/2010JB007721>.

485 **Zhang, Q.B.**, Zhao, J., 2014. A review of dynamic experimental techniques and mechanical
486 behaviour of rock materials, *Rock Mechanics and Rock Engineering*, 47, 1411-1478.

487

488

489 **Figure 1.** Natural *in-situ* shattered fault rocks. (a) Aerial view of the central and southern sectors
490 of the Foiana Fault Zone (Southern Alps, Italy; see inset on the top right): main fault strands
491 colored in red. Actual and inferred exposures of *in-situ* shattered dolostones along fault strike
492 were represented by blue areas; attitudes of the bedding around the fault were indicated with
493 white symbols. Low-hemisphere projection stereoplots represent joints attitude (both as poles
494 to planes and strike rose diagrams) moving from south (outcrop 1) to north (outcrop 2) along
495 fault strike. Joints were mainly parallel and perpendicular to the average fault strike. (b) View of
496 the Foiana Fault Zone (outcrop 1) exposed within a badland area. The exposed fault zone is >
497 300 m thick and consists of *in-situ* shattered rocks: intensely fragmented dolostones with little
498 to no evidence of shear strain (see inset on the right). (c-e) Rock fragments of the *in-situ*
499 shattered dolostones ranged from few centimeters down to few millimeters in size (c: hand
500 specimen photograph; e: tracings of the clasts at the thin section scale) and (d) were locally

501 characterized by micro-fragmentation zones affected by penetrative extensional fracturing
502 down to the micrometer scale. (f) Clast size distribution of *in-situ* shattered dolostones
503 measured at the thin section scale (investigated area $\sim 5 \text{ cm}^2$) in directions both parallel and
504 perpendicular to the fault strike. The two distributions had comparable slopes in the cumulative
505 number (N) vs. equivalent diameter logarithmic plot.

506

507 **Table 1.** List of uniaxial compression tests of this study. High-strain rate uniaxial compression
508 tests (#test: S1-S29) and low-strain rate uniaxial compression tests (#test: U1-U18). Symbols: d
509 = sample diameter; L = sample length; σ_{MAX} = peak axial stress; UCS = uniaxial compressive
510 strength; ϵ_{AMAX} = maximum axial strain; ϵ_{R} = residual axial strain; ϵ'_{MAX} = maximum strain rate;
511 ϵ'_{A} = applied strain rate; ϵ'_{C} = critical strain rate; E_{KIN} = input kinetic energy; E_{diss} = dissipated
512 strain energy; $E_{\text{diss-}\sigma_{\text{MAX}}}$ = dissipated strain energy up to the peak stress; E_{S} = surface fracture
513 energy; damage = sample damage state after the test. Damage: I = macroscopically intact; sp =
514 split; SH = shattered; F = incipient and prominent fragmentation; f = sample faulted; sp+f =
515 sample split and faulted. Indications: gages broken = strain gages broken during the test.

516

517 **Figure 2.** Low strain rate uniaxial compression tests. (a) Relation between uniaxial compressive
518 strength (UCS) and length to diameter ratio of the Mendola Formation rock cylinders tested at
519 strain rates of 6.7×10^{-6} and $6.7 \times 10^{-5} \text{ s}^{-1}$. UCS values were relatively scattered. In the photo,
520 macroscopic Andersonian-oriented fracture of a sample at the end of experiment U12. (b) Thin
521 section scan of the fractured sample U2 cut parallel to the loading direction (indicated by the
522 vertical black arrow). The sample was affected by sub-axial extensional fractures (longitudinal

523 splitting) more densely concentrated in the outer portion of the sample. The internal portion of
524 the sample U2 was affected by staircase arrays of oblique fractures (red in colour) and sub-axial
525 wing-like cracks. (c) Thin section scan of the fractured sample U2 cut perpendicular to the
526 loading direction. The sample was affected both by circular and radial extensional fractures in
527 its outer portion and tiny closed shear fractures associated to shear comminution within the
528 inner portion (see magnified SEM-BSE image in the inset).

529

530 **Figure 3.** High strain rate uniaxial compression tests. (a-c) Axial stress (blue in color line), axial
531 strain (red line) and strain rate (green line) histories of dynamically loaded samples and
532 associated damage states. σ_{MAX} and ϵ'_c indicate the peak axial stress and critical strain rate
533 respectively, following the terminology of Table 1. Shattered samples (Fig. 3c) were
534 characterized by a peculiar mechanical history compared to macroscopically intact and split
535 ones, with a double-pick strain rate path. The relative strain rate minimum corresponds to the
536 critical strain rate value for shattering in the test. (d) Stress vs. axial strain history of dynamically
537 loaded samples. Macroscopically intact and split samples showed a quasi-elastic to anelastic
538 behavior with residual strains <1%. Shattered samples accumulated residual strains always >
539 2%.

540

541 **Figure 4.** Deformation conditions for *in-situ* shattering. (a-c) Summary of high strain rate
542 compression experiments. Samples were shattered over strain rates of $\sim 120 \text{ s}^{-1}$ if the applied
543 peak stress was **on average** higher than the average UCS of the rock. Moreover experimentally

544 shattered samples showed a distinct clustering compared to the other samples in terms strain
545 energy dissipation.

546

547 **Figure 5.** *In-situ* microstructures of experimentally shattered samples. (a) X-ray
548 microtomography slice (sample S4) oriented perpendicular to the loading direction. Intense
549 rock fragmentation with fine-grained material (down to the micrometer scale) lining main
550 fractures is recognizable. Stress (blue line), strain (red line) and strain rate (green line) history of
551 sample S4 is reported in the top left inset. (b) SEM-BSE images mosaic of the shattered sample
552 S4 cut parallel to the loading direction (black in color arrow). Rock fragments were mostly few
553 millimeters in size, elongated in the loading direction and delimited by sub-parallel extensional
554 fractures. Pulverization (extensional fracturing down to the micrometer/crystal size scale)
555 occurred along the main fractures (some of the infilling material was lost during sample
556 polishing) and at the side where the stress wave entered the sample (see BSE-SEM magnified
557 image in the inset). (c-d) SEM-BSE images with details of rock pulverization by crystal boundary
558 breakage and fragmentation along cleavage planes.

559

560 **Figure 6.** Fracture pattern analysis. (a) X-ray tomography slices of the fracture pattern of a
561 quasi-statically fractured sample (test U4) and a dynamically shattered one (test S26) enhanced
562 by the application of a multiscale Hessian fracture filter (MSHFF) (Voorn et al., 2013). Since
563 quasi-statically loaded samples were larger compared to dynamically shattered ones, which
564 were even affected by dynamic confinement effects, both the entire (e.g., U4 in the figure) and
565 inner-core (e.g. U4sub in the figure) fracture pattern of quasi-statically fractured samples were

566 compared with dynamically shattered ones. The yellow dashed circumference delimits U4sub
567 which is comparable in size to sample S26 (the size comparison is highlighted by the two yellow
568 dashed lines). (b) Three dimensional fractures orientation ([poles to fracture planes](#); see Voorn
569 et al., 2015). Quasi-statically fractured samples (test U4) were affected by few circular fractures
570 and many Andersonian-oriented leading fractures (high hierarchy pattern). Dynamically
571 shattered samples (test S26) were affected by many fractures with variable strike orientation
572 and few leading ones (low hierarchy pattern). Volumetric fracture intensity was always larger
573 for dynamically shattered samples compared to quasi-statically fractured ones. (c) Three
574 dimensional fracture aperture distribution (number of voxel per aperture interval) was
575 significantly different (polymodal vs. unimodal) for quasi-static fractured samples compared to
576 dynamically shattered ones. (d) The two dimensional fracture skeleton of dynamically shattered
577 samples was characterized by a higher number of fracture branches compared to quasi-
578 statically fractured ones.

579

580 **Figure 7.** Two dimensional fragment size distribution of (i) natural *in-situ* shattered dolostones
581 measured on sections oriented both parallel and perpendicular to the average strike of the
582 Foiana Fault Zone, and (ii) experimental shattered dolostones measured on sections oriented
583 perpendicular to the loading direction. The distributions of both natural and experimental
584 samples were comparable (i.e. similar slopes), thus suggesting a common dynamic origin for
585 these shattered rocks. The clast size distributions were measured on equivalent surfaces of
586 0.78 cm^2 which was constrained by the dimension of the experimental samples.

587

588 **Figure 8.** Plot of dissipated strain energy up to the peak stress vs. maximum axial strain.
589 Experimentally shattered samples were characterized by much higher axial strains and slightly
590 higher strain energies dissipated up to the peak stress compared to the quasi-statically
591 fractured ones. Peculiarly shattered samples were produced only when an energy threshold of
592 $\sim 1.8 \text{ MJ/m}^3$ was overcome, which was significantly higher compared to the energy dissipated
593 by quasi-static compressive fracturing.

594

595 **Figure 9.** Fault rocks thickness vs. cumulative fault displacement scaling relations after Childs et
596 al. (2009) for various host rocks and fault kinematics (a,b). *In-situ* shattered dolostones at the
597 southern portion of the Foiana Fault Zone (displacement = 0.3-0.5 km, outcrop 1 in Fig.1a) were
598 > 300 m thick and lied out of the scaling trend displayed in the plots which are associated to
599 quasi-static fault growth models. Moving to the north (outcrop 2 in Fig.1a) the cumulative
600 displacement increased up to 1.6-1.8 km and the thickness of shattered rocks was ~ 100 m.
601 Here the scaling relation was more consistent with the one proposed by Childs et al. (2009).

Highlights

In-situ shattering is the result of high-energy dynamic rock fragmentation.

Quasi-static and dynamic fracture patterns are significantly different.

Experimental in-situ shattered dolostones resemble the natural ones.

In-situ shattered dolostones are geological markers of earthquake ruptures.

1 **Static versus dynamic fracturing in shallow carbonate fault zones**

2 Authors: Michele Fondriest^{1*}, Mai-Linh Doan², Frans Aben², Florian Fousseis³, Tomas M.
3 Mitchell⁴, Maarten Voorn⁵, Michele Secco^{6,7}, Giulio Di Toro^{1,8,9}

4

5 ¹ School of Earth, Atmospheric and Environmental Sciences, University of Manchester, M139PL,
6 Manchester, UK

7 ² ISTerre, Université Grenoble Alpes, CS 40700, GRENOBLE Cedex 9, FR

8 ³ School of Geosciences, University of Edinburgh, EH9 3FE, Edinburgh, UK

9 ⁴ Rock & Ice Physics Laboratory & UCL Seismolab, Department of Earth Sciences, University
10 College London, WC1E 6BT, London, UK

11 ⁵ Department of Geodynamics and Sedimentology, University of Vienna, Althanstrasse 14, 1090
12 Vienna, AUT - now at Baker Hughes.

13 ⁶ Department of Civil, Environmental and Architectural Engineering (ICEA), University of Padova,
14 via Francesco Marzolo 9, Padua, IT

15 ⁷ Inter-departmental Research Center for the Study of Cement Materials and Hydraulic Binders
16 (CIRCe), University of Padua, IT

17 ⁸ Dipartimento di Geoscienze, University of Padova, via G. Gradenigo 6, 35131, Padua, IT

18 ⁹ Istituto Nazionale di Geofisica e Vulcanologia (INGV), via di Vigna Murata 605, 00143, Rome, IT

19

20

21 **Keywords:** in-situ shattering, dynamic loading, earthquakes, quasi-static loading, carbonates,

22 fractures

23

24 **ABSTRACT**

25 Moderate to large earthquakes often nucleate within and propagate through carbonates in the
26 shallow crust. The occurrence of thick belts of low-strain fault-related breccias is relatively
27 common within carbonate damage zones and was generally interpreted in relation to the quasi-
28 static growth of faults. Here we report the occurrence of hundreds of meters thick belts of
29 intensely fragmented dolostones along a major transpressive fault zone in the Italian Southern
30 Alps. These fault rocks have been shattered *in-situ* with negligible shear strain accumulation.
31 The conditions of *in-situ* shattering were investigated by deforming the host dolostones in
32 uniaxial compression both under quasi-static (strain rate $\sim 10^{-5} \text{ s}^{-1}$) and dynamic (strain rate $>$
33 50 s^{-1}) loading. Dolostones deformed up to failure under low-strain rate were affected by single
34 to multiple discrete extensional fractures sub-parallel to the loading direction. Dolostones
35 deformed under high-strain rate were shattered above a strain rate threshold of $\sim 120 \text{ s}^{-1}$ and
36 peak stresses on average larger than the uniaxial compressive strength of the rock, whereas
37 they were split in few fragments or remained macroscopically intact at lower strain rates.
38 Fracture networks were investigated in three dimensions showing that low- and high-strain
39 rate damage patterns (fracture intensity, aperture, orientation) were significantly different,
40 with the latter being similar to that of natural *in-situ* shattered dolostones (i.e., comparable
41 fragment size distributions). *In-situ* shattered dolostones were thus interpreted as the result of
42 high energy dynamic fragmentation (dissipated strain energies $> 1.8 \text{ MJ/m}^3$) similarly to
43 pulverized rocks in crystalline lithologies. Given their seismic origin, the presence of *in-situ*

44 shattered dolostones can be used in earthquake hazard studies as evidence of the propagation
45 of seismic ruptures at shallow depths.

46

47 **1. INTRODUCTION**

48 Unstable fracture propagation and fragmentation are fundamental processes
49 dominating brittle deformation of solid materials loaded upon and beyond their elastic limit
50 (e.g., Scholz, 2002). The mechanics of fracturing is strongly controlled by the loading
51 configuration (tensile or compressive) since in tension a single crack can grow unstably (i.e.,
52 accelerating) until sample failure, whereas in compression a population of small cracks
53 propagates stably (i.e., steady growth rate) until stress interaction leads to instability and
54 sample failure (Ashby and Sammis, 1990). Fracture growth rates can range from stable quasi-
55 static low velocities to dynamic ones comparable or higher than the Rayleigh wave velocity of
56 the host material (e.g., Freund, 1990).

57 These considerations are particularly relevant when applied to rocks and fault zones in
58 which fractures are widespread. Experimental deformation of both rocks and analogue
59 materials (e.g., polymer composites) investigated the spectrum of propagation rates, from
60 stable to dynamic, for growing shear and tensile single fractures nucleated under various
61 loading configurations. As a result two major features, namely high angle tensile fractures and
62 macro- to micro branching were recognized to be exclusively associated to dynamic fracture
63 propagation (e.g., Sagy et al., 2001; Griffith et al., 2009; Fineberg et al., 1991, 1999). High angle
64 tensile fractures compare well with off-fault injection veins which are currently considered as
65 clear evidence of earthquake ruptures in the field, especially when filled with pseudotachylites

66 or fluidized fault rocks (Di Toro et al., 2005; Rowe and Griffith, 2015). Conversely this is not the
67 case for branching fractures which can even be induced by quasi-static loading (Sagy et al.,
68 2004). This means that besides investigating the growth velocity of single fractures, it is
69 important to determine the loading conditions (e.g. loading and strain rates) responsible for the
70 production of certain fracture patterns both in experiments and in nature.

71 The characterization of rock damage and the identification of dynamic signatures within
72 fault zones have fundamental implications for earthquake mechanics and in particular for the
73 constraint of energy budgets involved in seismic fracturing (e.g., Shipton et al., 2006; Pittarello
74 et al., 2008). To date rock pulverization (i.e., fragmentation down to the crystal size scale with
75 no shear strain accommodation) is the only large-scale macroscopic feature clearly relatable to
76 dynamic off-fault damage induced during the propagation of earthquake ruptures. Indeed
77 pulverized rocks have been reported in tens to hundreds of meters thick bands along major
78 faults (Dor et al., 2006, Mitchell et al., 2011) and were produced in the laboratory under high
79 strain rate loading conditions (Doan and Gary, 2009; Yuan et al., 2011). Fine-grained pulverized
80 rocks (sensu Brune et al., 2001) seem to be exclusively formed at shallow depth (less than 3 km)
81 within homogeneous stiff protoliths (mainly granitoids) while their occurrence was not
82 frequently reported for heterogeneous sedimentary covers. The latter is the case for
83 carbonates (i.e., limestones and dolostones), which are worldwide distributed lithologies
84 dominating the upper crust of many seismically active regions where moderate to large
85 magnitude earthquakes occur (e.g., 2008 Wenchuan Mw 7.9 and 2009 L'Aquila Mw 6.1
86 earthquakes; Burchfiel et al., 2008; Chiarabba et al., 2009). In particular, the occurrence of thick
87 belts (10-100s m) of low-strain, poorly distorted breccias (average size of rock fragments > 1

88 cm) is common within carbonate fault zones of various kinematics exhumed from a few
89 kilometers (e.g., Billi et al., 2003). These damage patterns were frequently interpreted in
90 relation to the quasi-static growth of fault zones characterized by the sequential formation and
91 activation of joints, pressure solution seams, veins, shear fractures during prolonged polyphasic
92 deformations (e.g., Salvini et al., 1999; Billi et al., 2003; Agosta et al., 2006).

93 Here we investigate the alternative possibility that some of these fragmented rocks in
94 carbonate fault zones may have a coseismic dynamic origin. We report the occurrence of thick
95 belts of *in-situ* shattered dolostones along a major transpressive fault zone in the Italian
96 Southern Alps and test the mechanical behavior of the dolomitic host rocks in compression over
97 a wide range of strain rates ($10^{-6} - 10^2 \text{ s}^{-1}$) to constrain the deformation conditions under which
98 *in-situ* shattering occurs. We used image analysis techniques to discriminate between quasi-
99 static and dynamic fracture patterns and inferred *in-situ* shattering as a dynamic coseismic
100 process. We finally consider the implications of our experimental results for the mechanics of
101 earthquakes and the scaling relationships of fault zones in carbonates.

102

103 **2. IN-SITU SHATTERED DOLOSTONES OF THE FOIANA FAULT ZONE**

104 The Foiana Fault Zone is a ~30 km long major sinistral transpressive fault exhumed from
105 < 2 km depth in the Italian Southern Alps. The fault zone crosscuts Permo-Triassic igneous and
106 sedimentary rocks, the latter including thick sequences of dolostones, with cumulative vertical
107 throw of 0.3-1.8 km (Fig. 1a) (Prosser, 1998). The host rock (Mendola Formation – peritidal
108 member) consists of light-gray sedimentary dolostones with cycles up to 0.6–1 m thick
109 characterized by stromatolitic laminations and planar trails of *fenestrae* (Avanzini et al., 2001;

110 Fondriest et al., 2015). The crystal size is in the range 20-300 μm , with the larger crystals filling
111 diagenetic pores (see Fondriest et al., 2015 for full description). Measured acoustic/elastic
112 properties of the host dolostones are: $V_p = 6.54 \pm 0.46$ km/s, $V_s = 3.64 \pm 0.15$ km/s, dynamic
113 Young modulus= 94.04 ± 9.04 GPa, while total Helium porosity is 1.7 ± 0.8 % (see
114 Supplementary Material).

115 The fault zone is exposed within badland areas and consists of > 300 m thick belts of intensely
116 fractured and fragmented dolostones which have been shattered *in-situ* with negligible shear
117 strain accumulation (Fig. 1b, see Fondriest et al., 2015). This is documented by the preservation
118 of primary sedimentary features (i.e., bedding surfaces, marly dolostone horizons and
119 stromatolitic laminations; see inset in Fig. 1b) even in the most highly fragmented rock bodies.
120 At the outcrop scale dolostones are reduced into fragments ranging from few centimeters
121 down to few millimeters in size separated by joints and extensional micro-fractures. Joints are
122 fault-related and are arranged in different sets (the most pervasive sets are parallel and
123 perpendicular to fault strike; rose diagrams in Fig. 1a) displaying complex cross-cutting/abutting
124 relations (Figs. 1a, b). At the meso- to micro-scale these rocks are affected by a pervasive and
125 non-hierarchical fracture pattern with variable fracture orientations, locally resulting in the
126 development of micro-fragmentation zones (fracture spacing < 1 mm) (Figs. 1c-e). Fragment
127 size distributions (FSD) (also named clast size distributions – CSD) measured in two dimensions
128 by manual drawing on thin section scans (area ~ 5 cm²) cover a clast size range of 0.05-7 mm
129 with average slopes of 1.2-1.3 in logarithmic plots (Figs. 1e-f) (see Supplementary Materials for
130 details). The slopes were computed in the narrower range of 0.4-2 mm where the curves had a
131 linear trend (Fig. 7), thus avoiding the external intervals. In fact, the latter are affected by bias

132 related to the spatial resolution of the images (data truncation) and to the finite size of the
133 analysis domain (data censoring). The clast size distributions determined on fault parallel and
134 fault perpendicular orientations were comparable (Fig.1f).

135

136 **3. METHODS**

137 To understand the origin of the *in-situ* shattered dolostones of the Foiana Fault Zone
138 low- to high- strain rate uniaxial compression experiments were performed on rock cylinders
139 cored from the Mendola Formation. Low-strain rate ($\sim 10^{-5} \text{ s}^{-1}$) tests were performed with a
140 uniaxial hydraulic test apparatus at the Rock and Ice Physics Laboratory at University College
141 London and a uniaxial hydraulic press at the Geoscience Department rock deformation
142 laboratory in Padova. High-strain rate ($> 50 \text{ s}^{-1}$) tests were conducted with a mini-Split
143 Hopkinson Pressure Bar (SHPB) at the ISTerre laboratory in Grenoble (Aben et al., 2016a).
144 Quasi-static uniaxial tests (N=16) were run both in displacement and stress control mode on 20
145 and 25 mm in diameter rock cylinders with various length/diameter ratios (~ 1 -2.4) (Table 1).
146 Dynamic SHPB tests (N=29) were run on samples with length/diameter ratio ~ 1 to reduce
147 inertia effects (Gama et al., 2004; Zhang and Zhao, 2014) and diameters of 10, 15 and 20 mm to
148 explore a wide range of peak stresses and strain rates (Table 1). Applied strain (i.e., loading
149 duration) was controlled by changing the length of the steel striker bar while striker impact
150 velocity was kept fixed around 5 m/s. Cardboard pulse shapers were used to guarantee stress
151 equilibrium conditions during the tests. Further details on the different apparatuses are
152 summarized in Supplementary Material.

153 Some of the samples were wrapped with a heat-shrinkable plastic jacket to be
154 recovered after the experiments (both quasi-static and dynamic loading tests) and analyze the
155 produced fracture pattern. Deformed samples were impregnated with epoxy and petrographic
156 thin sections cut both perpendicular and approximately parallel to the loading direction were
157 prepared for microstructural observations [optical microscopy (OM) and scanning electron
158 microscopy (SEM)]. Three dimensional fracture patterns were described through image analysis
159 techniques (software: FIJI, CTAn) applied to X-ray scan datasets acquired at different spatial
160 resolutions ($8 \times 8 \times 8 \mu\text{m}^3$ and $23 \times 23 \times 23 \mu\text{m}^3$ per voxel), while fragment size distribution (FSD)
161 was determined in two dimensions both for natural and experimental shattered rocks (see
162 Supplementary Material for details).

163

164 **4. RESULTS**

165 *4.1. MECHANICAL DATA AND DAMAGE STATES*

166 Quasi-static uniaxial compression tests were performed on both jacketed and
167 unjacketed samples with varying length to diameter ratio at strain rates of $6.7 \times 10^{-6} \text{ s}^{-1}$ and
168 $6.7 \times 10^{-5} \text{ s}^{-1}$. Measured uniaxial strengths (UCS) and static Young moduli (average values: $227.3 \pm$
169 45 MPa and $64.1 \pm 18 \text{ GPa}$ respectively, see Supplementary Material) were relatively scattered
170 and did not show any correlation with either strain rate or sample geometry (Fig. 2a). The
171 observed variability was likely a consequence of the mechanical heterogeneity of the tested
172 rock. Samples loaded up to failure accumulated permanent axial strains of 0.2-0.7% while
173 elastic strain energy ($E_{diss-\sigma_{MAX}}$ in Table 1, calculated as the area below the “axial stress vs. axial
174 strain” curve) dissipated up to the peak stress was $0.4\text{-}1 \text{ MJ/m}^3$. The common failure mode was

175 longitudinal “sub-axial” splitting (*sensu* Holzhausen and Johnson, 1979) with fractures oriented
176 parallel or at small angle ($<10^\circ$) to the loading direction and cutting through the entire sample.
177 Many of these fractures were concentrated in the outer portion of the sample, where radial
178 expansion is expected to be higher, and had a curvilinear trace in plain view (exfoliation
179 extensional fractures) (Figs. 2b, c). Instead, the central portion of the sample consisted of a
180 continuous "pillar" affected by short (<5 mm trace length) closed shear fractures and staircase
181 arrays of oblique fractures and sub-axial wing cracks (Figs. 2b, c). In some cases the
182 development of a through going Andersonian-oriented leading shear fracture (i.e., sample
183 faulting) was observed (inset in Fig. 2a).

184 Dynamic SHPB tests performed on both jacketed and unjacketed samples spanned peak
185 stresses of 60-360 MPa, axial strains of 0.3-3% and peak strain rates of $140-450\text{ s}^{-1}$ (Table 1,
186 Figs. 3-4). The stress, strain and strain rate histories of the dynamically loaded samples highlight
187 the applied peak stress and the critical strain rate (ϵ'_c in Table 1) as primary factors in
188 controlling the mechanical behavior and the ultimate damage state of the samples. As
189 previously observed by Aben et al. (2016a) the critical strain rate ϵ'_c represents the plateau or
190 inflection point value of the strain rate vs. time curve and roughly matches in time with the
191 applied peak stress (Figs. 3a,b). When recovered after loading the samples were (i)
192 macroscopically intact (Fig. 3a), (ii) split in few pieces (Fig. 3b), or (iii) intensely fragmented (Fig.
193 3c). Samples loaded at critical strain rates of $\sim 20\text{ s}^{-1}$ and peak stresses of 100-150 MPa (below
194 the average UCS limit, Figs. 4a, b) showed a quasi-elastic stress-strain behavior (residual strains
195 $\sim 0.2\%$, Figs. 3a, d) and were macroscopically intact or split if they contained preexisting
196 heterogeneities (e.g., sub-axial veins, Fig. 3a). Samples loaded at critical strain rates $\sim 50\text{ s}^{-1}$ and

197 peak stresses ≤ 200 MPa (around the average UCS limit, Figs. 4a, b) accumulated residual strains
198 of 0.4-0.6% (Figs. 3b, d) and were split or macroscopically intact (Fig.3b). Samples loaded at
199 critical strain rates $> 120 \text{ s}^{-1}$ and peak stresses of ≥ 200 MPa (around and over the average UCS
200 limit, Figs. 4a, b) accumulated residual strains $> 2\%$ (Figs. 3c, d) and were typically intensely
201 fragmented (Fig. 3c). In this case the strain rate at which fragmentation occurred was a relative
202 minimum in the strain rate vs. time curve, preceding a second strain rate peak occurring during
203 sample unloading (Aben et al., 2016a) (Fig.3c). Dissipated strain energy during fragmentation
204 was in the range 1.5-2.8 MJ/m³ (E_{diss} in Table 1), almost 30% of the kinetic energy transferred by
205 the striker impact to the steel bar (E_{kin} in Table 1, calculated as $E_{kin} = 0.5 \times m \times v^2$, where m is the
206 striker mass and v the striker impact velocity; Fig. 4c). These samples were reduced into a non-
207 cohesive material with angular rock fragments mostly of few millimeters in size (Fig. 3c).
208 Looking at *in-situ* microstructures (X-ray tomography and microscopy on thin sections), the
209 fragments were elongated in the loading direction and delimited by subparallel extensional
210 fractures crosscut by a few orthogonal ones (Figs. 5a, b). Diffuse tensile microfracturing
211 exploiting both cleavage planes and grain boundaries occurred along the main fractures and at
212 the side where the stress wave entered the sample (Figs. 5c, d). Such microstructures, coupled
213 with the general absence of shear strain, are very similar in natural *in-situ* shattered dolostones
214 (compare Figs. 5a, d with Figs. 1c-e).

215 4.2. FRACTURE PATTERN ANALYSIS

216 The three-dimensional fracture patterns of quasi-statically and dynamically deformed
217 samples were quantified and compared by using image analysis applied to X-ray computed
218 tomography datasets (for details see Supplementary Material) (Figs. 6a-c). To extract the

219 fracture network from the tomographic images we used the approach implemented by Voorn
220 et al. (2013) (multiscale Hessian fracture filter – MSHFF) for the software FIJI (Schindelin et al.,
221 2012), which was optimized for the enhancement and segmentation of narrow planar features
222 such as fractures (see Supplementary Material). Further properties of the fracture network such
223 as fracture intensity, bulk fracture orientation and aperture were determined after Voorn et al.
224 (2015) using both FIJI and CTAn software (for details see Supplementary Material). The fracture
225 skeletons were analyzed in two dimensions on slices oriented orthogonal to the loading
226 direction.

227 Volumetric fracture intensity values (total fracture surface/sample volume) were
228 significantly higher for dynamically shattered samples ($\sim 4.0 \text{ mm}^{-1}$) compared to quasi-statically
229 fractured ones ($\sim 1.4 \text{ mm}^{-1}$) (Fig. 6b). Bulk fracture aperture followed a unimodal distribution
230 (modal value $\sim 0.03 \text{ mm}$ for samples S4 and S26, Fig. 6c) in shattered samples while it was
231 characterized by a polymodal distribution (modal values $> 0.1 \text{ mm}$ for sample U4, Fig. 6c) in
232 quasi-statically fractured samples. In both cases fractures were oriented almost parallel to the
233 loading direction (Fig. 6b). In terms of strike fractures generated under dynamic loading were
234 quite scattered or arranged in a orthorhombic geometry (“low hierarchy” fracture pattern),
235 while fractures produced under quasi-static loading were clustered around the orientation of
236 few leading fractures (“high hierarchy” fracture pattern) (Figs. 6a, b). Overall the fracture
237 patterns produced by dynamic loading were characterized by a much higher number of fracture
238 branches and intersections compared to the quasi-static ones (Fig. 6d).

239 4.3. FRAGMENT SIZE DISTRIBUTIONS OF THE SHATTERED DOLOSTONES

240 Fragment size distributions (FSD) of experimental shattered dolostones were
241 determined in two dimensions by manual drawing on X-ray tomographic images over an area of
242 $\sim 0.8 \text{ cm}^2$ which was constrained by the dimensions of the experimental samples (for details
243 see Supplementary Material). To allow a comparison, the FSDs of natural shattered dolostones
244 (see Fig.1f) were recalculated on the same smaller analysis domains (area $\sim 0.8 \text{ cm}^2$) (Fig.7). The
245 resulting FDSs of both natural and experimental shattered dolostones were comparable in the
246 size range 0.01-4 mm with an average slope of 0.73 ± 0.14 in logarithmic plots (Fig.7). The slopes
247 were computed in the narrower range of 0.1-1 mm where the curves had a linear trend (Fig.7),
248 thus avoiding the external intervals which are affected by bias related to the spatial resolution
249 of the images (data truncation) and to the finite size of the analysis domain (data censoring).
250 Recalculated slopes (D) of natural shattered dolostones are smaller (~ 0.7 on average; Fig.7)
251 than the ones determined on larger analysis domains (~ 1.2 on average; Fig.1f). The different
252 slopes in the fragment distributions plots are certainly due to the undersampling effects
253 associated to the reduction of the analysed sampled area. However, the diverse slopes might
254 also suggest that the FSDs of these rocks are neither spatial heterogeneous nor self-similar. To
255 investigate this hypothesis it would be necessary to determine the fragment size distributions
256 over a much larger size range (i.e. three to four orders of magnitude).

257 **5. DISCUSSION AND CONCLUSIONS**

258 *5.1. ENERGY SINKS AND DAMAGE*

259 Experimental results indicate that intensely fragmented *in-situ* shattered dolostones
260 were produced in compression when the applied critical strain rate was $> 120 \text{ s}^{-1}$ and the peak
261 stress was on average larger than the uniaxial compressive strength of the rock (227.3 ± 45

262 MPa) (Figs. 4a-c). In particular, when we considered the strain energy dissipated in the sample
263 up to the peak stress ($E_{diss-\sigma MAX}$ in Table 1), the occurrence of an energy threshold of ~ 1.8
264 MJ/m³, above which *in-situ* shattering start to develop, was evident (Fig.8). Interestingly this
265 energy threshold was larger than the total energy dissipated in the pulverization of crystalline
266 rocks such as quartz-monzonite (~ 1.5 MJ/m³; Aben et al., 2016a) and calcitic marble (~ 1.1
267 MJ/m³; Doan and Billi, 2011). Estimates of surface fracture energies for the shattered samples
268 (E_S in Table 1) were 40-80% of dissipated strain energy (E_{diss} in Table 1, see Supplementary
269 Material). The dynamically fragmented samples had distinctive characteristics compared to
270 quasi-statically fractured ones: (i) higher fracture intensity, (ii) narrower fractures, (iii) low-
271 hierarchy and high-complexity of the fracture pattern (Figs. 6a-d). All these characteristics are
272 consistent with high strain rate loading during which the energy supply to the sample is too fast
273 to be dissipated by only few fractures: this results in intense fragmentation of the rock (Grady
274 and Kipp, 1989; Bhat et al., 2012; Doan and d'Hour, 2012, Aben et al, 2016b). On the other
275 hand quasi-statically loaded samples displayed typical low-rate propagation features such as
276 subaxial wing cracks growing at the tips of inclined fractures (e.g., Ashby and Sammis, 1990).
277 Instead, the relatively abundance of curvilinear fractures in the outer portion of the samples
278 was due to non-uniform stress distribution and lack of confinement during the tests (Peng and
279 Johnson, 1972), and has to be considered as an artifact when compared with natural fault
280 rocks. This was not the case for dynamically loaded samples, which were instead affected by
281 radial fractures due to the occurrence of dynamic confinement (radial confinement up to ~ 0.5
282 MPa, see Supplementary Material) at high loading rates, when the effect of material inertia
283 becomes significant (Doan and Gary, 2009; Chen, 2011).

284 5.2. *IN-SITU SHATTERING: NATURE VS. LAB*

285 *In-situ* shattered dolostones were exclusively produced at high dynamic loading rates in
286 the laboratory. The deformation conditions determined for shattering in dolostones (critical
287 strain rate $> 120 \text{ s}^{-1}$, axial strain $> 2\%$, Fig. 4) were comparable to those associated to
288 pulverization of homogeneous crystalline rocks (i.e., granite, quartz-monzonite, calcitic marble;
289 Doan and Gary, 2009; Yuan et al., 2011, Doan and Billi, 2011; Aben et al., 2016a) and considered
290 to be transiently achieved in the fault wall rocks during the propagation of an earthquake
291 rupture (e.g., Ben-Zion and Shi, 2005; Reches and Dewers, 2005). Moreover, in contrast to the
292 quasi-statically deformed samples, experimentally shattered dolostones showed striking
293 similarities with the natural ones of the Foiana Fault Zone: (i) two dimensional FSDs determined
294 at the scale of the experimental samples (area $\sim 0.8 \text{ cm}^2$) were comparable (average slope =
295 0.73 ± 0.14 , size range = 0.01-4 mm) (Figs. 7), (ii) rock fragments were frequently exploded with
296 no evidence of shear strain, (iii) pervasive extensional fracturing locally occurred down to the
297 micrometer scale (microfragmentation domains) (Figs. 1c-e and Figs. 5a-d). All these
298 observations suggest that also natural *in-situ* shattered dolostones had a dynamic origin
299 potentially related to multiple off-fault coseismic stress-wave loadings (Fondriest et al., 2015).

300 5.3 SHATTERED DOLOSTONES AND HYDRAULIC DILATION BRECCIAS

301 The shattered dolostones of the Foiana Fault Zone are characterized by a well-fitted
302 jigsaw puzzle texture which in most of the cases is comparable to that of the *crackle breccias*
303 defined by Woodcock and Mort (2008) in their “non-genetic” fault breccias classification (more
304 than 75% of sample area covered by clasts $> 2 \text{ mm}$ in size). This type of fault breccia was
305 originally described in the dolomitic host rocks of the Dent Fault (northwest England) and

306 characterized by extensive infill of the fracture network by hydrothermal carbonate cement
307 (Tarasewicz et al., 2005; Woodcock et al., 2006). In a similar way many *crackle* and *shatter*
308 breccias described in the mining literature as fault-related were associated to hydraulic
309 implosion mechanisms and frequently cemented by the deposition of hydrothermal minerals
310 (e.g., Phillips, 1972; Mitcham, 1974; Sibson, 1986). According to Sibson (1986) implosive
311 brecciation is a dynamic coseismic process generated by a sudden collapse of the wall rock at
312 dilational fault jogs (mainly during rupture arrest) coupled with the generation of strong pore
313 fluid pressure gradients. Compared to implosion hydraulic breccias, the shattered dolostones of
314 the Foiana Fault Zone (i) were observed in different fault zone sections (straight fault segments
315 and restraining bends; Fig. 1a) and, (ii) did not show presence of veins or cement filling the
316 fracture network (see Fondriest et al., 2015 for details). Basing on the experimental results
317 presented in this study (all the experiments were performed in “dry”- room humidity
318 conditions, see section 3) *in-situ* shattered dolostones of the Foiana Fault Zone are the result of
319 off-fault coseismic damage due to the propagation of multiple earthquake ruptures in a relative
320 fluid-poor environment. This hypothesis might be furtherly reinforced by the occurrence of
321 other structural features such as highly localized mirror-like fault surfaces lined by thin
322 ultracataclastic layers, sharply truncating the shattered dolostones and previously interpreted as
323 evidence of extreme coseismic shear strain localization based on field, microstructural and
324 experimental observations (see for more details Fondriest et al., 2013, 2015).

325 5.4. IMPLICATIONS FOR SCALING RELATIONS IN FAULT ZONES

326 The experimental observations presented here open the possibility to reinterpret the
327 origin of low-strain breccias (10-100s m thick) frequently associated with fault zones in

328 carbonates and classically interpreted in relation to the “slow” quasi-static growth of faults (i.e.,
329 nucleation and interaction of various generations of joints, pressure solution seams and shear
330 fractures; e.g., Salvini et al., 1999; Billi et al., 2003; Agosta et al., 2006). Many of these breccias,
331 especially within stiff dolomitic protoliths, might instead be produced by dynamic shattering
332 during the propagation of earthquake ruptures and then be more efficiently affected by
333 dissolution-precipitation and mass transfer processes during the post- or inter-seismic periods
334 (e.g., Gratier et al. 2014). Following this line of thought most of the volume of these fault zones
335 would be generated during earthquakes as it is also suggested by aftershocks spatial
336 distributions along active seismogenic faults (e.g., Valoroso et al., 2013). Moreover faults
337 associated with *in-situ* shattered fault rocks are frequently characterized by thickness vs.
338 displacement (t/d) ratios which are significantly higher (i.e., $t/d \sim 1$) compared to the classical
339 scaling relations estimated for relatively “simpler” fault zones (i.e., characterized by discrete
340 fault surfaces and well described by the “*damage zone-fault core*” model of Caine et al., 2010)
341 according to purely geometric quasi-static growth models ($t/d \sim 0.1$; e.g., Childs et al., 2009).
342 This is particularly evident within near-tip fault sections, as in the case of the southern sector of
343 the Foiana Fault Zone, where cumulative displacement tends to be low and the effects of slip
344 accumulation by stable sliding are likely to be minimized (Fig. 9). Therefore the occurrence of
345 high thickness vs. displacement ratios, coupled with the presence of *in-situ* shattered fault
346 rocks, can potentially be used to assess (i) the propagation of earthquake ruptures at shallow
347 depth along carbonate fault zones, and (ii) the hazard related to seismogenic sources with
348 incomplete earthquake catalogs. As a consequence the accurate mapping of the distribution of
349 *in-situ* shattered fault rocks along seismogenic fault zones and the precise quantification of

350 their fracture intensity represent the base for future robust evaluations of the actual
351 contribution of surface fracture energy in the earthquake energy balance at shallow depth (i.e.,
352 < 3 km).

353

354 **Acknowledgments**

355 MF performed all the experiments in collaboration with MLD and FA (SHPB tests) and TMM
356 (uniaxial compression tests), the microstructural analyses in collaboration with FF and MS (X-
357 ray microtomography) and MV (fracture pattern analysis), and wrote the first version of the
358 manuscript. All the authors contributed to revise the final version of the manuscript. The
359 detailed comments of Shalev Siman-Tov and Tom Blenkinsop greatly improved the quality of
360 the manuscript. MF thanks Marco Avanzini, who introduced him to the outcrops of the Foiana
361 Fault Zone; Leonardo Tauro, Elena Masiero, Joséphine Gervin, Matteo Parisatto, Mark Jefferd,
362 Lorenzo Raccagni, Bruno Ciervo, Stefano Castelli and Luca Peruzzo for technical and
363 microanalytical support. MF and GDT acknowledge the European Research Consolidator Grant
364 (No. 614705) NOFEAR. MS thanks Fondazione Cassa di Risparmio di Padova e Rovigo (CaRiPaRo)
365 for financial support. TMM acknowledges support from NERC grant ref NE/M004716/1.

366

367 **Reference list**

368 **Aben, F.M.**, Doan, M.-L., Mitchell, T.M., Toussaint, R., Reuschlé, T., Fondriest, M., Gratier, J.-P.,
369 Renard, F., 2016a. Dynamic fracturing by successive coseismic loadings leads to pulverization in
370 active fault zones, *J. Geophys. Res. Solid Earth*, 121, 2338–2360, doi:10.1002/2015JB012542.

371 **Aben, F.M.**, Doan M.-L., Gratier, J.-P., Renard, F., 2016b. Coseismic damage generation and
372 pulverization in fault zones: insights from dynamic Split-Hopkinson Pressure Bar experiments.
373 In: "Evolution of Fault Zone Properties and Dynamic Processes during Seismic Rupture", edited
374 by M.Y. Thomas, H.S. Bhat, T.M. Mitchell. (in press)

375 **Agosta, F.**, Aydin, A., 2006. Architecture and deformation mechanism of a basin-
376 bounding normal fault in Mesozoic platform carbonates, central Italy. *J. Struct. Geol.* 28
377 (8),1445–1467.

378 **Ahsby, M.F.** and Sammis, C. G., 1990. The damage mechanics of brittle solids in compression,
379 *Pure and Applied Geophysics*, 133, 489-521.

380 **Avanzini, M.**, Bargossi, G.M., Castiglioni, G.B., Dalmeri, G., Eccel, E., Mancabelli, A. , Morelli, C.,
381 Neri, C., Picotti, V., Prosser, G., Sartori, G., Zambotti, G., 2001. Carta Geologica della Provincia
382 di Trento, tav. 26 III Fondo (a scala 1:25.000) con Note illustrative, 159 pp., Provincia Autonoma
383 di Trento, Servizio Geologico.

384 **Ben-Zion, Y.** and Shi, Z., 2005. Dynamic rupture on a material interface with spontaneous
385 generation of plastic strain in the bulk, *Earth and Planetary Science Letters*, 236, 486-496.

386 **Bhat, H.S.**, Rosakis, A.J., Sammis, C. G., 2012. A micromechanics based constitutive model for
387 brittle failure at high strain rates, *Journal of Applied Mechanics*, doi:10.1115/1.4005897.

388 **Billi, A.**, Salvini, F., Storti, F., 2003. The damage zone-fault core transition in carbonate rocks:
389 implications for fault growth, structure and permeability. *J. Struct. Geol.* 25 (11), 1779–1794.

390 **Brune, J.**, 2001. Fault normal dynamic loading and unloading: an explanation for non-gouge
391 rock powder and lack of fault-parallel shear bands along the San Andreas Fault. *EOS Trans. Am.*
392 *Geophys. Union* 82, 47

393 **Burchfiel, B.C.**, Royden, L.H., Van der Hilst, R.D., Hager, B.H., Chen, Z., King, R., Li, C., Lu, Y.,
394 Kirby, E., 2008. A geological and geophysical context for the Wenchuan earthquake of 12 May
395 2008, Sichuan, People's Republic of China, *GSA today*, 18, 5.

396 **Chiarabba, C.** et al., 2009. The 2009 L'Aquila (central Italy) M_w 6.3 earthquake: main shock and
397 aftershocks. *Geophysical Research Letters*, <http://dx.doi.org/10.1029/2009GL039627>.

398 **Chen, W.W.** and Song, B., 2011. Split Hopkinson (Kolsky) Bar - Design, Testing and Applications,
399 Mechanical Engineering Series, Springer.

400 **Childs, C.**, Manzocchi, T., Walsh, J.J., Bonson, C.G., Nicol, A., Schöpfer, M.P.J., 2009. A geometric
401 model of fault zone and fault rock thickness variations. *Journal of Structural Geology* 31,
402 117e127.

403 **Di Toro G.**, Nielsen, S., Pennacchioni, G., 2005. Earthquake rupture dynamics frozen in exhumed
404 ancient faults. *Nature*, 436, 1009-1012.

405 **Doan, M.-L.**, Billi, A., 2011. High strain rate damage of Carrara marble. *Geophys. Res. Lett.* 38
406 (38), L19302. <http://dx.doi.org/10.1029/2011GL049169>.

407 **Doan, M.-L.** and D'Hour, V., 2012. Effect of initial damage on rock pulverization along faults, *J.*
408 *Struct. Geol.*, 45, 113–124, doi:10.1016/j.jsg.2012.05.006.

409 **Doan, M.-L.** and Gary, G., 2009. Rock pulverisation at high strain rate near the San Andreas
410 Fault. *Nat. Geosci.* 2, 709–712.

411 **Dor, O.**, Ben-Zion, Y., Rockwell, T.K., Brune, J., 2006b. Pulverized rocks in the Mojave section of
412 the San Andreas fault zone. *Earth Planet. Sci. Lett.* 245, 642–654.

413 **Fineberg, J.**, Gross, S., Marder, M., and H. Swinney, 1992. Instability in the propagation of fast
414 cracks, *Physical Reviews*, B45, 5146-5154.

415 **Fineberg, J.**, and Marder, M., 1999. Instability in Dynamic Fracture, *Physics Reports*, 313, 1-108.

416 **Fondriest, M.**, Smith, S.A.F., Candela, T., Nielsen, S.B., Mair, K., Di Toro, G., 2013. Mirror-like
417 faults and power dissipation during earthquakes, *Geology*, 41, 1175-1178.

418 **Fondriest, M.**, Aretusini, S., Di Toro, G., Smith, S.A.F., 2015. Fracturing and rock pulverization
419 along an exhumed seismogenic fault zone in dolostones: The Foiana Fault Zone (Southern Alps,
420 Italy), *Tectonophysics*, 654, 56-74.

421 **Freund, L.B.** (1990), *Dynamic Fracture Mechanics*, Cambridge Univ. Press, Cambridge.

422 **Gama, B.A.**, Lopatnikov, S.L., Gillespie, W.J., 2004. Hopkinson bar experimental technique: A
423 critical review, *Appl. Mech. Rev.*, 57(4), 223, doi:10.1115/1.1704626.

424 **Grady, D.E.**, and Kipp, M.E., 1987. Dynamic rock fragmentation, in *Fracture Mechanics of Rock*,
425 Atkinson B. K. ed., Academic Press Geology Series, London.

426 **Gratier, J.-P.**, Renard, F., Vial, B., 2014. Postseismic pressure solution creep: Evidence and
427 time-dependent change from dynamic indenting experiments, *Journal of Geophysical Research*,
428 119, 2764-2779.

429 **Griffith, W.A.**, Rosakis, A., Pollard, D.D., Ko, C.W., 2009. Dynamic rupture experiments elucidate
430 tensile crack development during propagating earthquake ruptures, *Geology*, 37, 795-798.

431 **Holzhausen, G.R.**, and Johnson, A.M., 1979. Analyses of longitudinal splitting of uniaxially
432 compressed rock cylinders, *International Journal of Rock Mechanics and Mining Sciences &*
433 *Geomechanics Abstracts*, 16, 163-177.

434 **Mitcham, T.W.**, 1974. Origin of breccia pipes, *Econ. Geol.*, 69, 412-413.

435 **Mitchell, T.M.**, Ben-Zion, Y., Shimamoto, T., 2011. Pulverized fault rocks and damage
436 asymmetry along the Arima Takatsuki Tectonic Line, Japan, *Earth Planet. Sci. Lett.* 308, 284–297.

437 **Peng, S.**, and Johnson, A.M., 1972. Crack growth and faulting in cylindrical specimens of
438 Chelmsford granite, *International Journal of Rock Mechanics and Mining Sciences &*
439 *Geomechanics Abstracts*, doi:10.1016/0148 9062(72)90050-2.

440 **Phillips, W.J.**, 1972. Hydraulic fracturing and mineralization. *J. Geol. Soc. Lond.*, 128, 337-359.

441 **Pittarello, L.**, Di Toro, G., Bizzarri, A., Pennacchioni, G., Hadizadeh, J., Cocco, M., 2008. Energy
442 partitioning during seismic slip in pseudotachylyte-bearing faults (Gole Larghe Fault, Adamello,
443 Italy), *Earth and Planetary Science Letters*, 269, 131-139.

444 **Prosser, G.**, 1998. Strike-slip movements and thrusting along a transpressive fault zone: the
445 North Giudicarie line (Insubric line, northern Italy), *Tectonics*, 17, 921–937.

446 **Reches, Z.**, Dewers, T.A., 2005. Gouge formation by dynamic pulverization during earthquake
447 rupture, *Earth and Planetary Science Letters*, 235, 361-374.

448 **Rowe, C.D.**, and Griffith, W.A., 2015. Do faults preserve a record of seismic slip: A second
449 opinion, *J. Struct. Geol.*, 78, doi:10.1016/j.jsg.2015.06.006.

450 **Sagy, A.**, Reches, Z., Roman, I., 2001. Dynamic fracturing: field and experimental observations,
451 *J. Struct. Geol.*, 23, 1223-1239.

452 **Sagy, A.**, Fineberg, J., Reches, Z., 2004. Shatter cones: Branched, rapid fractures formed by
453 shock impact, *J. Geophys. Res. B Solid Earth*, 109(10), 1–20, doi:10.1029/2004JB003016.

454 **Salvini, F.**, Billi, A., Wise, D.U., 1999. Strike-slip fault-propagation cleavage in carbonate rocks:
455 the Mattinata Fault Zone, Southern Apennines, Italy, *J. Struct. Geol.*, 21, 1731-1749.

456 **Schindelin, J.**, Arganda Carreras, I., Frise, E., Kaynig, V., Longair, M., Pietzsch, T., Preibisch, S.,
457 Rueden, C., Saalfeld, S., Schmid, B., Tinevez, J.Y., White, D.J., Hartenstein, V., Eliceiri, K.,

458 Tomancak, P., Cardona, A., 2012. Fiji:an open-source platform for biological-image analysis.
459 Nat. Methods 9(7), 676–682, <http://dx.doi.org/10.1038/nmeth.2019..>

460 **Scholz, C.H.**, 2002. The Mechanics of Earthquakes and Faulting. Cambridge University Press,
461 Cambridge.

462 **Shipton, Z.K.**, Evans, J.P., Abercrombie, R.E., Brodsky, E.E., 2006. The missing sinks: Slip
463 localization in faults, damage zones, and the seismic energy budget. In “Earthquakes: radiated
464 energy and the physics of faulting”, American Geophysical Union monograph, 217-222.

465 **Sibson, R.H.**, 1986. Brecciation processes in fault zones: inferences from earthquake rupturing,
466 Pure Appl. Geophys., 124, 159-175.

467 **Tarasewicz, J.P.T.**, Woodcock, N.H., Dickson, J.A.D., 2005. Carbonate dilation breccias:
468 examples from the damage zone to the Dent Fault, northwest England, Geol. Soc. Am. Bull.,
469 117, 736-745.

470 **Valoroso, L.**, Chiaraluce, L., Piccinini, D., Di Stefano, R., Schaff, D., Waldhauser, F., 2013.
471 Radiography of a normal fault system by 64,000 high-precision earthquake locations: the 2009
472 L'Aquila (central Italy) case study. J. Geophys. Res. Solid Earth.
473 <http://dx.doi.org/10.1002/jgrb.50130>.

474 **Voorn, M.**, Exner, U., Rath, A., 2013. Multiscale Hessian fracture filtering for the enhancement
475 and segmentation of narrow fractures in 3D image data, Comput. Geosci., 57,44–53.

476 **Voorn, M.**, Exner, U., Barnhoorn, A., Baud, B., Reuschlé, T., 2015. Porosity, permeability and 3D
477 fracture network characterisation of dolomite reservoir rock samples, Journal of Petroleum
478 Science and Engineering, 127, 270-285.

479 **Woodcock, N.H.**, Omma, J.E., Dickson, J.A.D., 2006. Chaotic breccia along the Dent Fault, NW
480 England: implosion or collapse of a fault void?, *J. Geol. Soc. Lond.*, 163, 431-446.

481 **Woodcock, N.H.**, Mort, K., 2008. Classification of fault breccias and related fault rocks, *Geol.*
482 *Mag.*, 145, 435-440.

483 **Yuan, F.**, Prakash, V., Tullis, T., 2011. Origin of pulverized rocks during earthquake fault rupture.
484 *J. Geophys. Res.* 116, B06309. <http://dx.doi.org/10.1029/2010JB007721>.

485 **Zhang, Q.B.**, Zhao, J., 2014. A review of dynamic experimental techniques and mechanical
486 behaviour of rock materials, *Rock Mechanics and Rock Engineering*, 47, 1411-1478.

487

488

489 **Figure 1.** Natural *in-situ* shattered fault rocks. (a) Aerial view of the central and southern sectors
490 of the Foiana Fault Zone (Southern Alps, Italy; see inset on the top right): main fault strands
491 colored in red. Actual and inferred exposures of *in-situ* shattered dolostones along fault strike
492 were represented by blue areas; attitudes of the bedding around the fault were indicated with
493 white symbols. Low-hemisphere projection stereoplots represent joints attitude (both as poles
494 to planes and strike rose diagrams) moving from south (outcrop 1) to north (outcrop 2) along
495 fault strike. Joints were mainly parallel and perpendicular to the average fault strike. (b) View of
496 the Foiana Fault Zone (outcrop 1) exposed within a badland area. The exposed fault zone is >
497 300 m thick and consists of *in-situ* shattered rocks: intensely fragmented dolostones with little
498 to no evidence of shear strain (see inset on the right). (c-e) Rock fragments of the *in-situ*
499 shattered dolostones ranged from few centimeters down to few millimeters in size (c: hand
500 specimen photograph; e: tracings of the clasts at the thin section scale) and (d) were locally

501 characterized by micro-fragmentation zones affected by penetrative extensional fracturing
502 down to the micrometer scale. (f) Clast size distribution of *in-situ* shattered dolostones
503 measured at the thin section scale (investigated area $\sim 5 \text{ cm}^2$) in directions both parallel and
504 perpendicular to the fault strike. The two distributions had comparable slopes in the cumulative
505 number (N) vs. equivalent diameter logarithmic plot.

506

507 **Table 1.** List of uniaxial compression tests of this study. High-strain rate uniaxial compression
508 tests (#test: S1-S29) and low-strain rate uniaxial compression tests (#test: U1-U18). Symbols: d
509 = sample diameter; L = sample length; σ_{MAX} = peak axial stress; UCS = uniaxial compressive
510 strength; ϵ_{AMAX} = maximum axial strain; ϵ_{R} = residual axial strain; ϵ'_{MAX} = maximum strain rate;
511 ϵ'_{A} = applied strain rate; ϵ'_{C} = critical strain rate; E_{KIN} = input kinetic energy; E_{diss} = dissipated
512 strain energy; $E_{\text{diss-}\sigma_{\text{MAX}}}$ = dissipated strain energy up to the peak stress; E_{S} = surface fracture
513 energy; damage = sample damage state after the test. Damage: I = macroscopically intact; sp =
514 split; SH = shattered; F = incipient and prominent fragmentation; f = sample faulted; sp+f =
515 sample split and faulted. Indications: gages broken = strain gages broken during the test.

516

517 **Figure 2.** Low strain rate uniaxial compression tests. (a) Relation between uniaxial compressive
518 strength (UCS) and length to diameter ratio of the Mendola Formation rock cylinders tested at
519 strain rates of 6.7×10^{-6} and $6.7 \times 10^{-5} \text{ s}^{-1}$. UCS values were relatively scattered. In the photo,
520 macroscopic Andersonian-oriented fracture of a sample at the end of experiment U12. (b) Thin
521 section scan of the fractured sample U2 cut parallel to the loading direction (indicated by the
522 vertical black arrow). The sample was affected by sub-axial extensional fractures (longitudinal

523 splitting) more densely concentrated in the outer portion of the sample. The internal portion of
524 the sample U2 was affected by staircase arrays of oblique fractures (red in colour) and sub-axial
525 wing-like cracks. (c) Thin section scan of the fractured sample U2 cut perpendicular to the
526 loading direction. The sample was affected both by circular and radial extensional fractures in
527 its outer portion and tiny closed shear fractures associated to shear comminution within the
528 inner portion (see magnified SEM-BSE image in the inset).

529

530 **Figure 3.** High strain rate uniaxial compression tests. (a-c) Axial stress (blue in color line), axial
531 strain (red line) and strain rate (green line) histories of dynamically loaded samples and
532 associated damage states. σ_{MAX} and ϵ'_c indicate the peak axial stress and critical strain rate
533 respectively, following the terminology of Table 1. Shattered samples (Fig. 3c) were
534 characterized by a peculiar mechanical history compared to macroscopically intact and split
535 ones, with a double-pick strain rate path. The relative strain rate minimum corresponds to the
536 critical strain rate value for shattering in the test. (d) Stress vs. axial strain history of dynamically
537 loaded samples. Macroscopically intact and split samples showed a quasi-elastic to anelastic
538 behavior with residual strains <1%. Shattered samples accumulated residual strains always >
539 2%.

540

541 **Figure 4.** Deformation conditions for *in-situ* shattering. (a-c) Summary of high strain rate
542 compression experiments. Samples were shattered over strain rates of $\sim 120 \text{ s}^{-1}$ if the applied
543 peak stress was on average higher than the average UCS of the rock. Moreover experimentally

544 shattered samples showed a distinct clustering compared to the other samples in terms strain
545 energy dissipation.

546

547 **Figure 5.** *In-situ* microstructures of experimentally shattered samples. (a) X-ray
548 microtomography slice (sample S4) oriented perpendicular to the loading direction. Intense
549 rock fragmentation with fine-grained material (down to the micrometer scale) lining main
550 fractures is recognizable. Stress (blue line), strain (red line) and strain rate (green line) history of
551 sample S4 is reported in the top left inset. (b) SEM-BSE images mosaic of the shattered sample
552 S4 cut parallel to the loading direction (black in color arrow). Rock fragments were mostly few
553 millimeters in size, elongated in the loading direction and delimited by sub-parallel extensional
554 fractures. Pulverization (extensional fracturing down to the micrometer/crystal size scale)
555 occurred along the main fractures (some of the infilling material was lost during sample
556 polishing) and at the side where the stress wave entered the sample (see BSE-SEM magnified
557 image in the inset). (c-d) SEM-BSE images with details of rock pulverization by crystal boundary
558 breakage and fragmentation along cleavage planes.

559

560 **Figure 6.** Fracture pattern analysis. (a) X-ray tomography slices of the fracture pattern of a
561 quasi-statically fractured sample (test U4) and a dynamically shattered one (test S26) enhanced
562 by the application of a multiscale Hessian fracture filter (MSHFF) (Voorn et al., 2013). Since
563 quasi-statically loaded samples were larger compared to dynamically shattered ones, which
564 were even affected by dynamic confinement effects, both the entire (e.g., U4 in the figure) and
565 inner-core (e.g. U4sub in the figure) fracture pattern of quasi-statically fractured samples were

566 compared with dynamically shattered ones. The yellow dashed circumference delimits U4sub
567 which is comparable in size to sample S26 (the size comparison is highlighted by the two yellow
568 dashed lines). (b) Three dimensional fractures orientation (poles to fracture planes; see Voorn
569 et al., 2015). Quasi-statically fractured samples (test U4) were affected by few circular fractures
570 and many Andersonian-oriented leading fractures (high hierarchy pattern). Dynamically
571 shattered samples (test S26) were affected by many fractures with variable strike orientation
572 and few leading ones (low hierarchy pattern). Volumetric fracture intensity was always larger
573 for dynamically shattered samples compared to quasi-statically fractured ones. (c) Three
574 dimensional fracture aperture distribution (number of voxel per aperture interval) was
575 significantly different (polymodal vs. unimodal) for quasi-static fractured samples compared to
576 dynamically shattered ones. (d) The two dimensional fracture skeleton of dynamically shattered
577 samples was characterized by a higher number of fracture branches compared to quasi-
578 statically fractured ones.

579

580 **Figure 7.** Two dimensional fragment size distribution of (i) natural *in-situ* shattered dolostones
581 measured on sections oriented both parallel and perpendicular to the average strike of the
582 Foiana Fault Zone, and (ii) experimental shattered dolostones measured on sections oriented
583 perpendicular to the loading direction. The distributions of both natural and experimental
584 samples were comparable (i.e. similar slopes), thus suggesting a common dynamic origin for
585 these shattered rocks. The clast size distributions were measured on equivalent surfaces of
586 0.78 cm^2 which was constrained by the dimension of the experimental samples.

587

588 **Figure 8.** Plot of dissipated strain energy up to the peak stress vs. maximum axial strain.
589 Experimentally shattered samples were characterized by much higher axial strains and slightly
590 higher strain energies dissipated up to the peak stress compared to the quasi-statically
591 fractured ones. Peculiarly shattered samples were produced only when an energy threshold of
592 $\sim 1.8 \text{ MJ/m}^3$ was overcome, which was significantly higher compared to the energy dissipated
593 by quasi-static compressive fracturing.

594

595 **Figure 9.** Fault rocks thickness vs. cumulative fault displacement scaling relations after Childs et
596 al. (2009) for various host rocks and fault kinematics (a,b). *In-situ* shattered dolostones at the
597 southern portion of the Foiana Fault Zone (displacement = 0.3-0.5 km, outcrop 1 in Fig.1a) were
598 > 300 m thick and lied out of the scaling trend displayed in the plots which are associated to
599 quasi-static fault growth models. Moving to the north (outcrop 2 in Fig.1a) the cumulative
600 displacement increased up to 1.6-1.8 km and the thickness of shattered rocks was ~ 100 m.
601 Here the scaling relation was more consistent with the one proposed by Childs et al. (2009).

Figure

[Click here to download high resolution image](#)

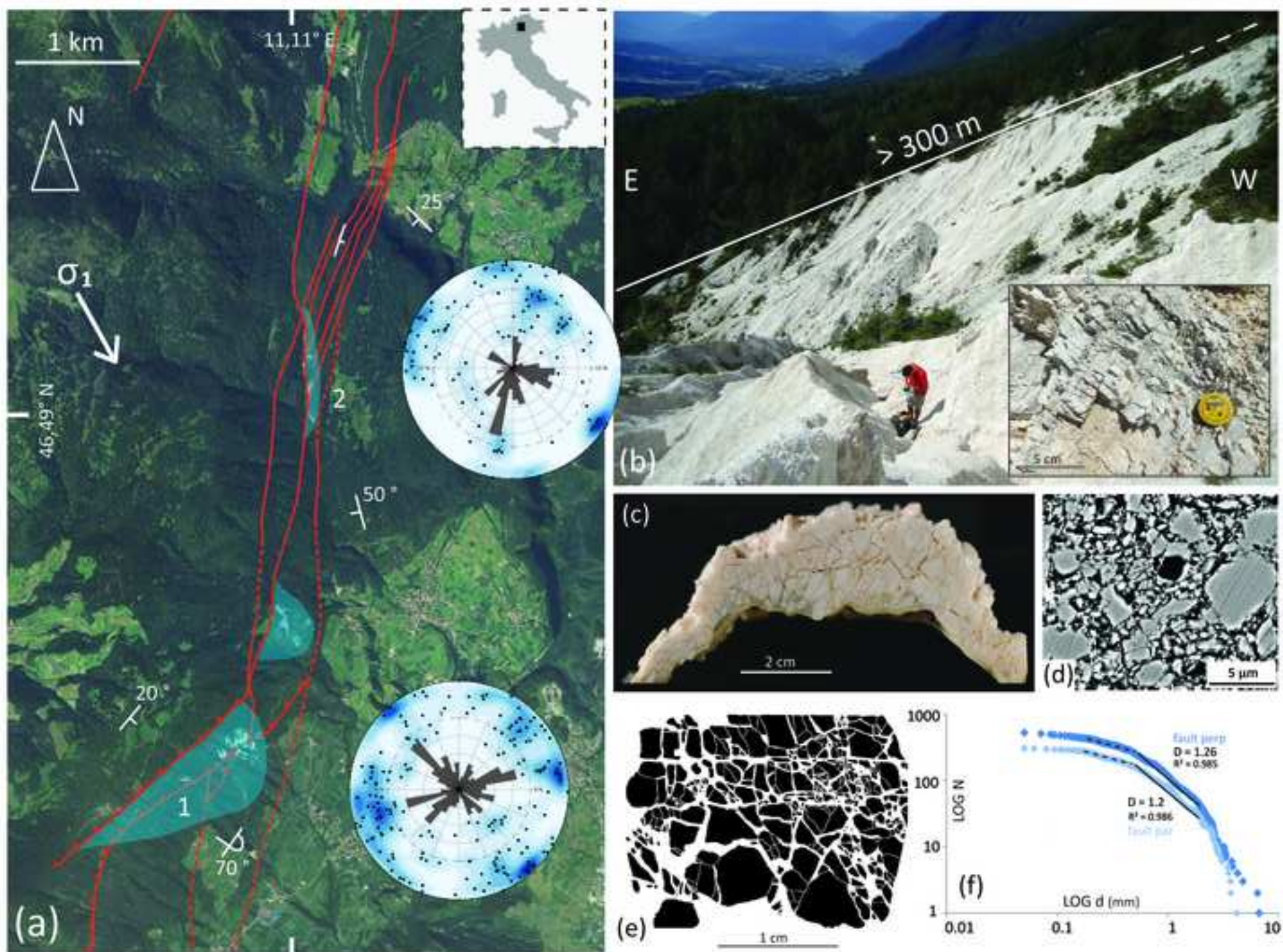
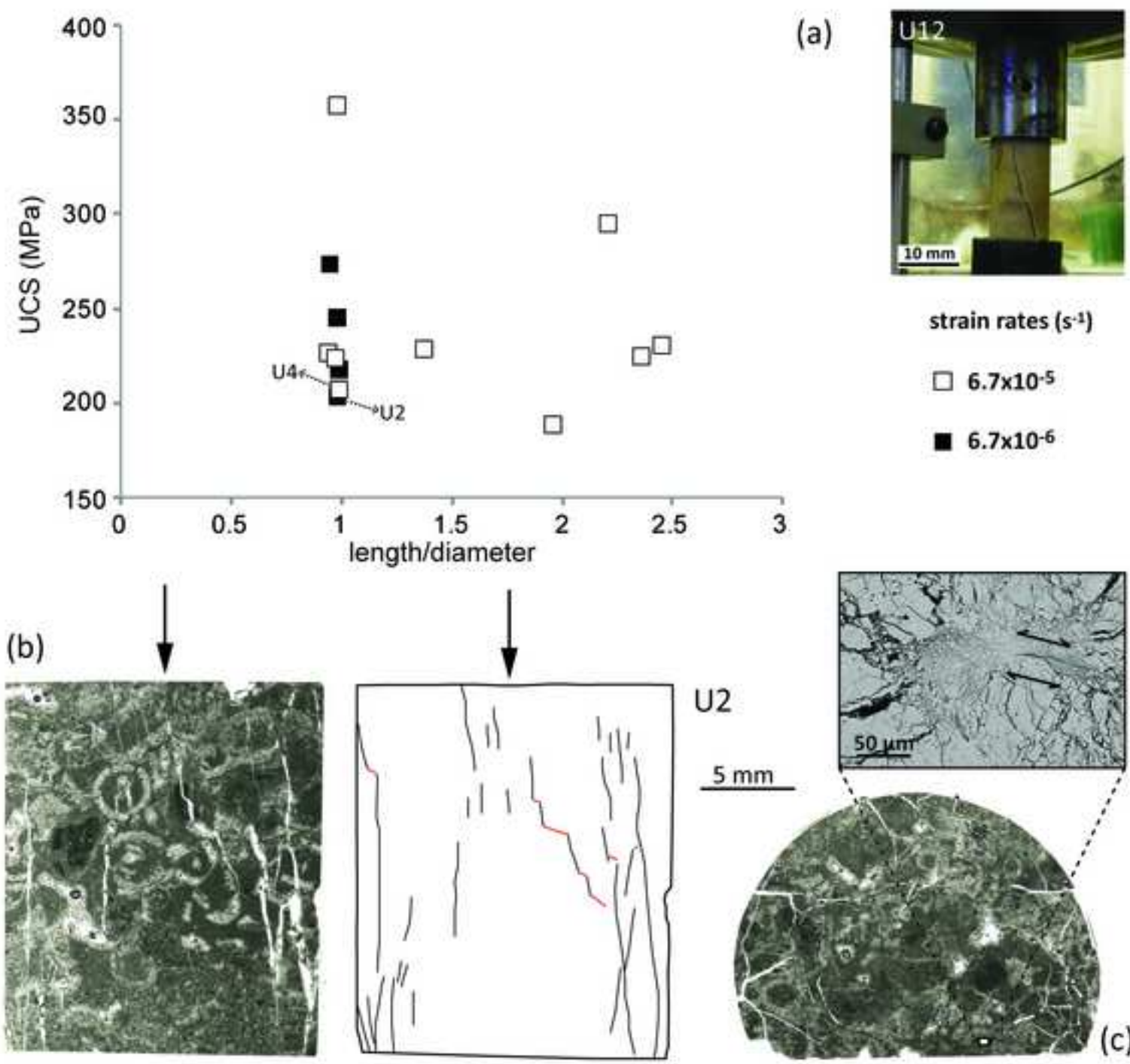
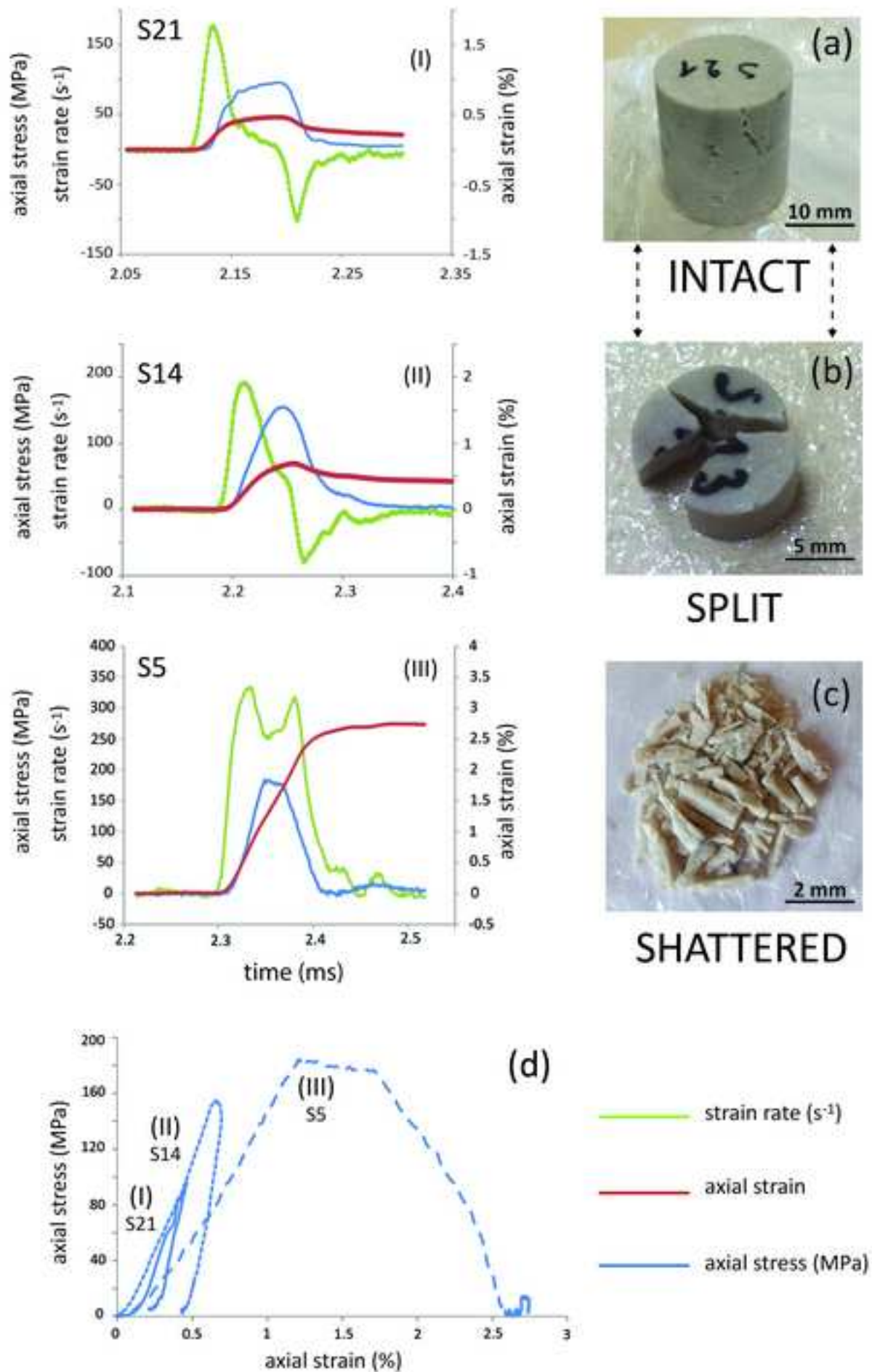


Figure
[Click here to download high resolution image](#)



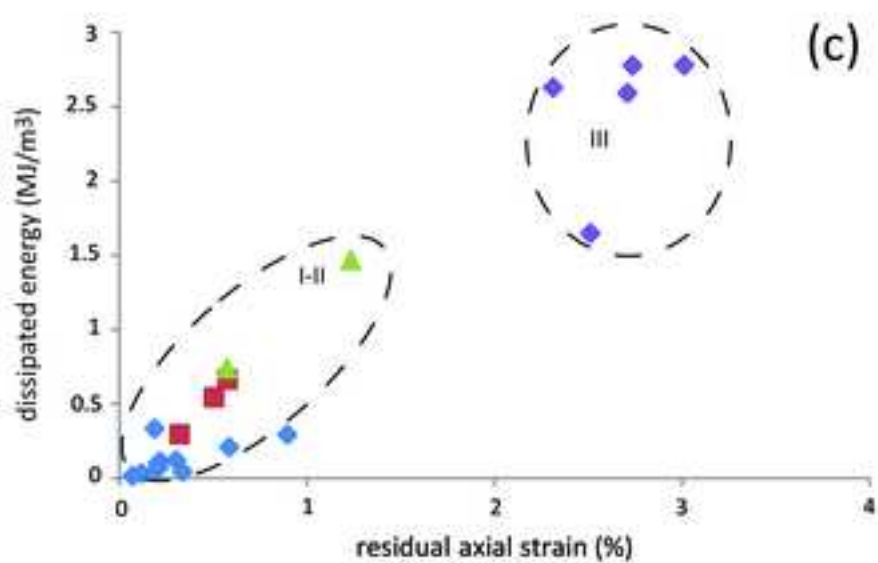
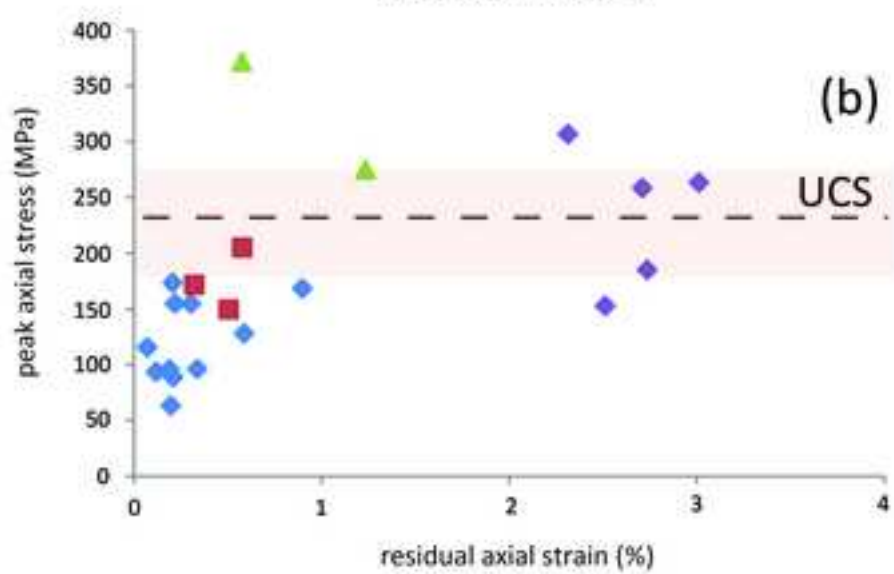
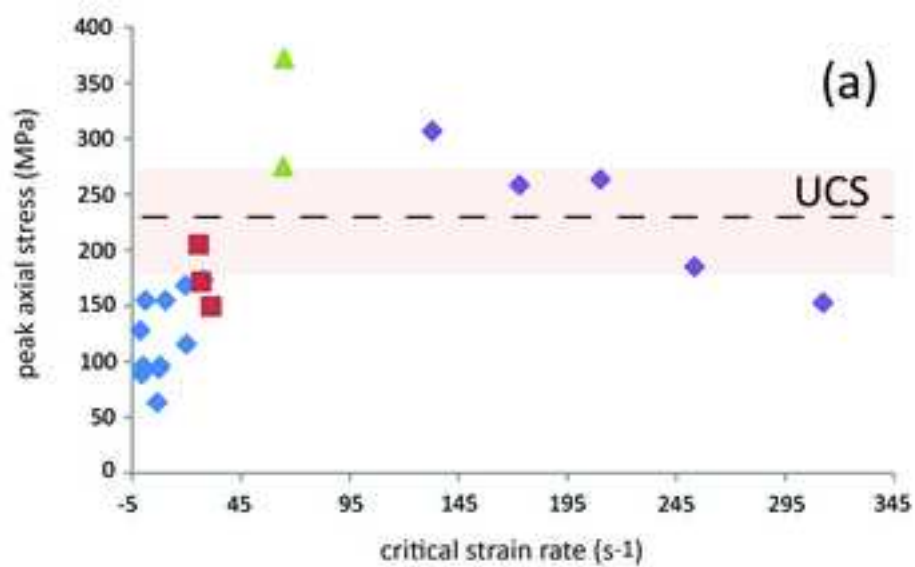
Figure

[Click here to download high resolution image](#)



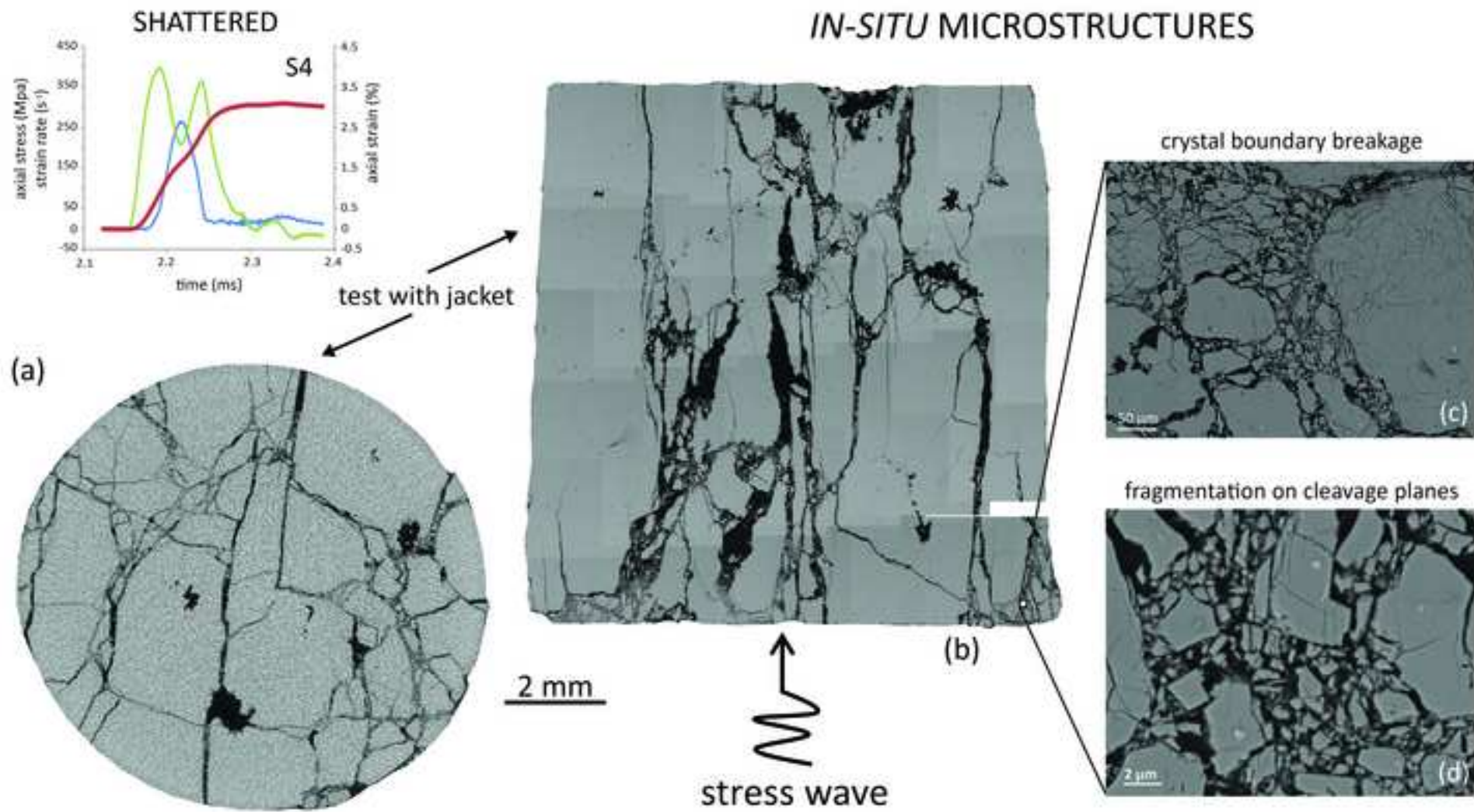
Figure

[Click here to download high resolution image](#)



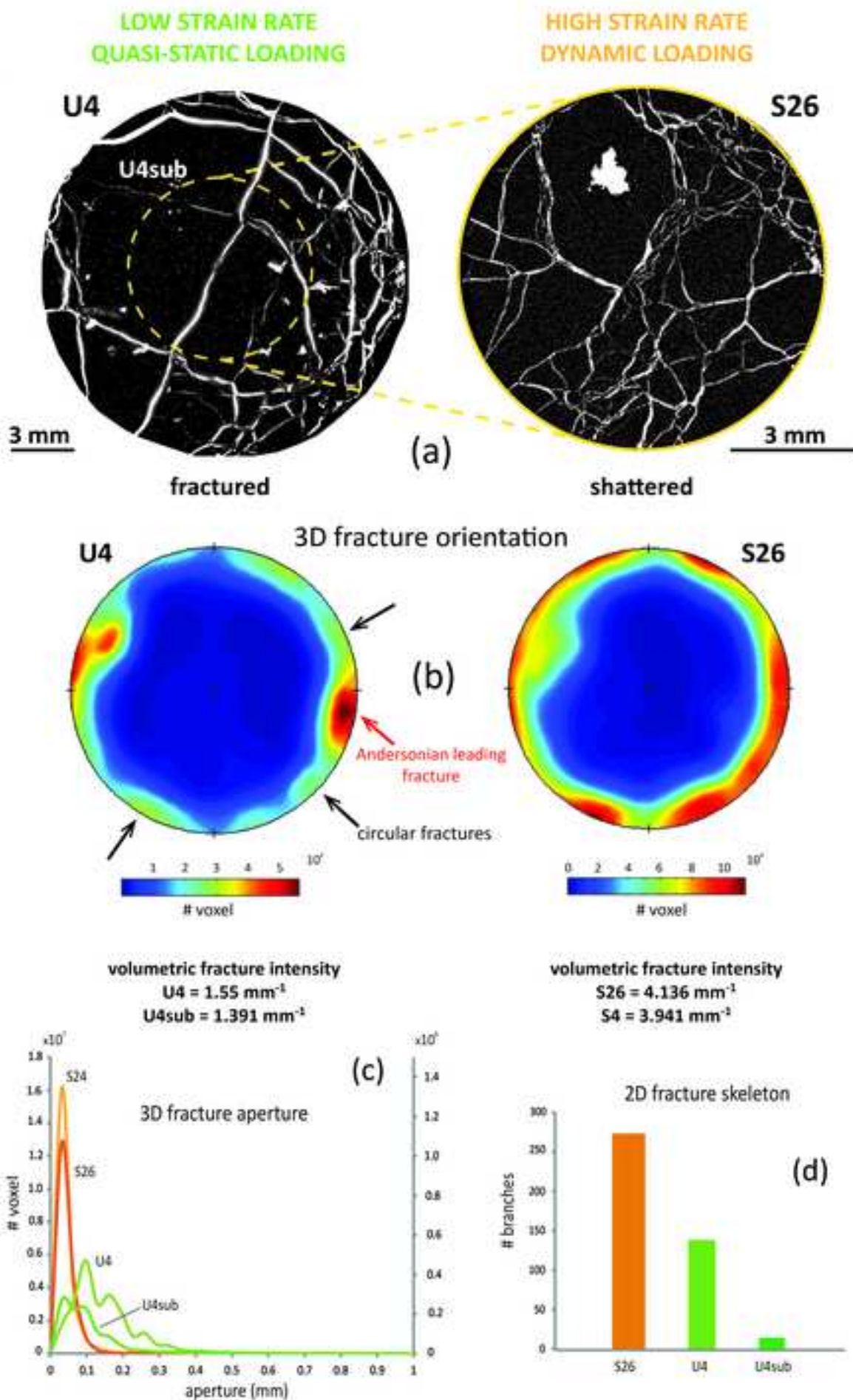
◆ intact ■ split ▲ starts to fragment ◆ shattered

Figure
[Click here to download high resolution image](#)



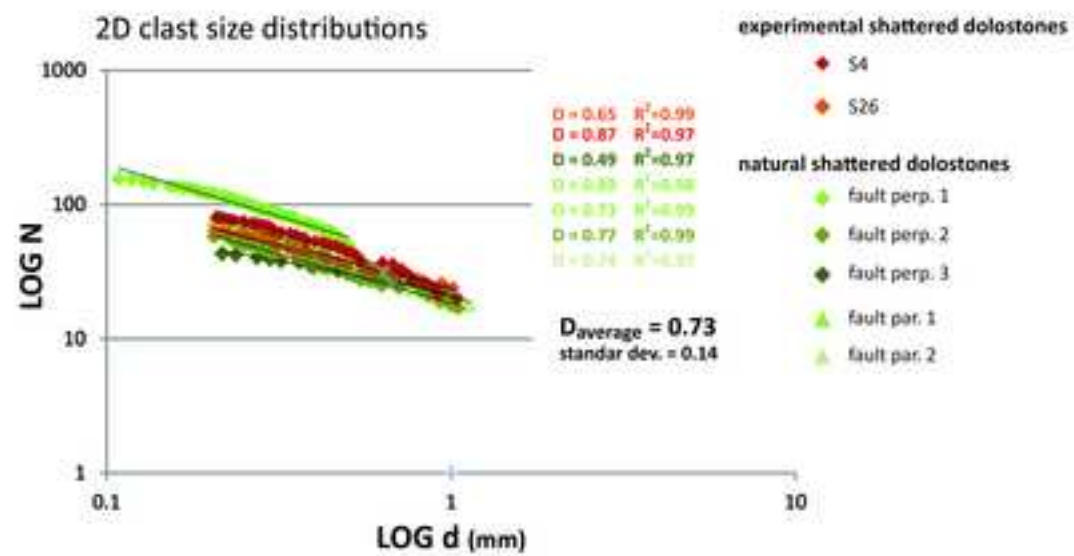
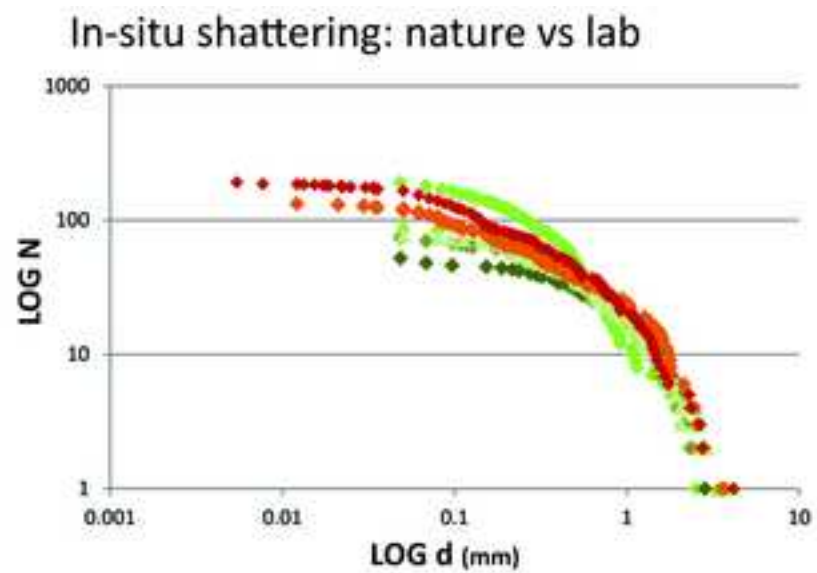
Figure

[Click here to download high resolution image](#)



Figure

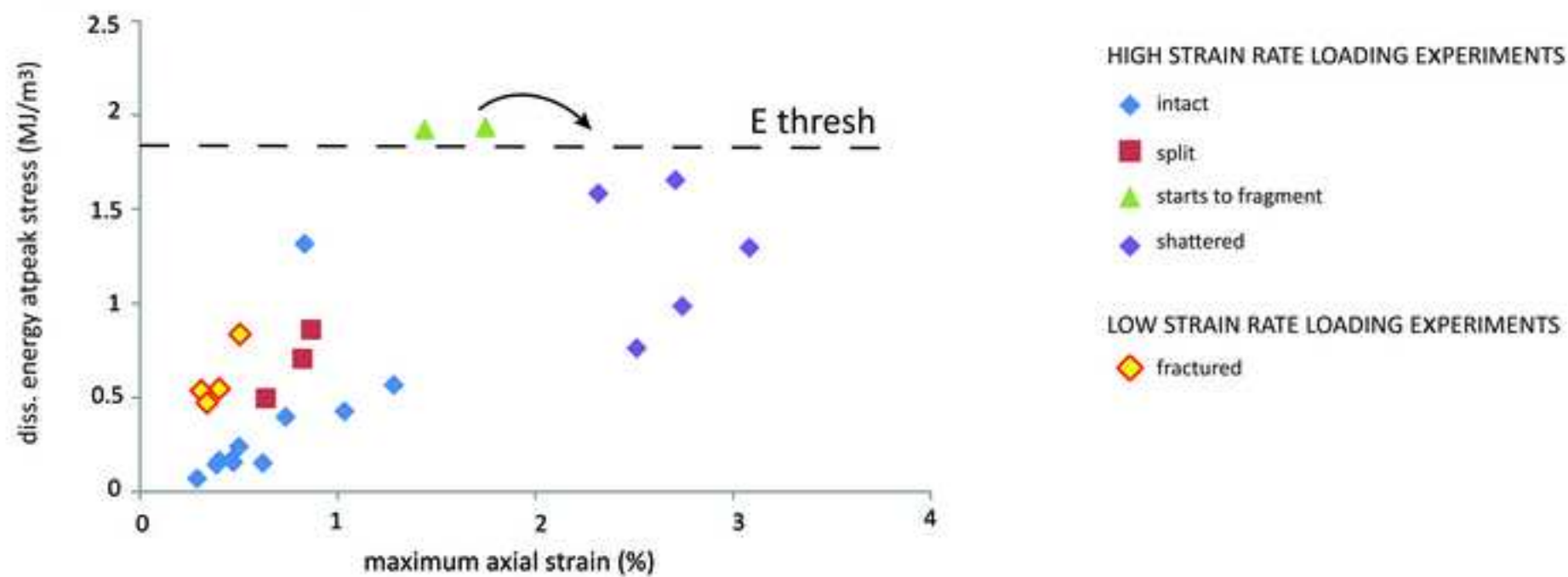
[Click here to download high resolution image](#)



Figure

[Click here to download high resolution image](#)

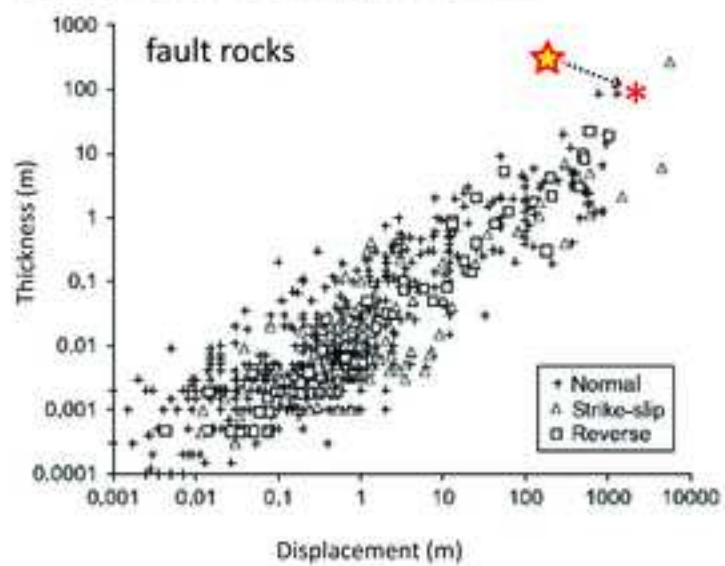
Energy sinks and damage



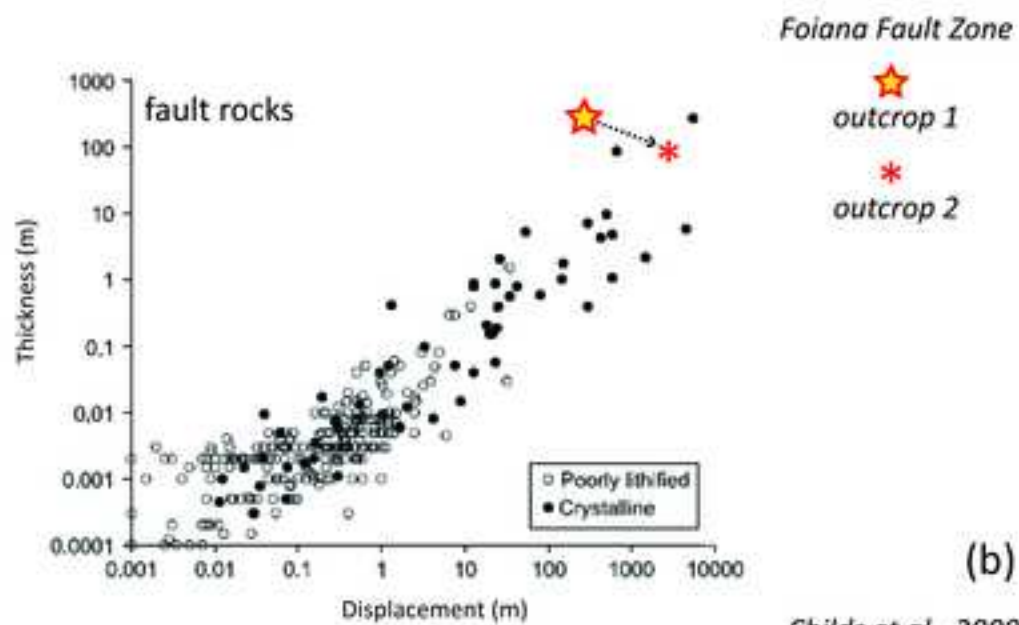
Figure

[Click here to download high resolution image](#)

Fault zones scaling relations



(a)



(b)

Childs et al., 2009

Figure (high-resolution)

[Click here to download Figure \(high-resolution\): Figure_1.jpg](#)

Figure (high-resolution)

[Click here to download Figure \(high-resolution\): 2.tif](#)

Figure (high-resolution)

[Click here to download Figure \(high-resolution\): 3.jpg](#)

Figure (high-resolution)

[Click here to download Figure \(high-resolution\): 4.jpg](#)

Figure (high-resolution)

[Click here to download Figure \(high-resolution\): 5.jpg](#)

Figure (high-resolution)

[Click here to download Figure \(high-resolution\): 6.jpg](#)

Figure (high-resolution)

[Click here to download Figure \(high-resolution\): Figure_7.jpg](#)

Figure (high-resolution)

[Click here to download Figure \(high-resolution\): Figure_8.jpg](#)

Figure (high-resolution)

[Click here to download Figure \(high-resolution\): 9.jpg](#)

Table

[Click here to download high resolution image](#)

# test	d (mm)	L (mm)	σ_{MAX} (Mpa)	ϵ_{AMAX} (%)	ϵ_R (%)	ϵ'_{MAX} (s^{-1})	ϵ'_c (s^{-1})	E_{LIN} (MJ)	E_{DISS} (MJ/m ³)	$E_{DISS-\sigma MAX}$ (MJ/m ³)	E_s (MJ/m ³)	damage
S1	15.0	15.0	168.3	1.3	0.9	312.8	19.6	6.5	0.29	0.56	-	I
S2	15.0	14.9	171.7	0.6	0.3	185.7	26.7	0.0	0.30	0.49	-	sp
S3	15.0	14.8	149.5	0.8	0.5	144.7	31.3	0.0	0.54	0.71	-	sp
S4	9.6	9.4	263.3	3.1	3.0	397.2	210.2	6.7	2.78	1.29	1.18	SH
S5	9.8	9.2	185.0	2.7	2.7	334.8	253.4	5.5	2.78	0.98	-	SH
S6	-	-	-	-	-	-	-	-	-	-	-	F
S7	9.6	9.5	275.0	1.7	1.2	306.1	64.9	5.6	1.47	1.93	-	I
S8	9.4	9.6	258.3	2.7	2.7	313.1	173.0	6.2	2.59	1.65	-	F
S9	9.6	9.5	-	-	-	-	-	-	-	-	-	I
S10	9.6	9.7	152.7	2.5	2.5	415.8	312.5	4.7	1.65	0.76	-	SH
S11	9.6	9.2	371.7	1.4	0.6	449.3	64.5	5.0	0.74	1.92	-	I
S12	9.6	9.5	127.8	1.0	0.6	293.7	-1.3	1.5	0.21	0.42	-	F
S13	9.6	9.3	205.0	0.9	0.6	237.6	25.7	2.0	0.66	0.86	-	sp
S14	14.9	14.5	154.7	0.7	0.4	191.2	47.4	5.0	0.38	0.49	-	sp
S15	15.0	15.0	173.3	0.7	0.3	209.2	1.3	5.4	0.12	0.40	-	I
S16	14.9	14.8	115.7	0.5	0.2	180.7	10.4	2.2	0.11	0.24	-	I
S17	14.9	14.7	-	-	-	-	-	-	-	-	-	I
S18	14.9	15.0	88.7	0.4	0.2	143.9	27.9	1.5	0.10	0.16	-	I
S19	20.9	20.4	63.3	0.3	0.1	161.2	19.9	2.3	0.01	0.07	-	I
S20	20.9	20.5	-	-	-	-	-	-	-	-	-	I
S21	20.9	20.8	96.2	0.5	0.2	177.0	-0.5	7.1	0.07	0.17	-	I
S22	20.9	20.4	93.5	0.5	0.2	187.1	6.7	6.9	0.06	0.15	-	I
S23	-	-	-	-	-	-	-	-	-	-	-	I
S24	20.9	20.9	95.8	0.6	0.3	204.9	8.0	5.7	0.04	0.15	-	I
S25	20.9	21.0	96.7	0.4	0.1	168.7	7.4	5.8	0.03	0.14	-	I
S26	9.6	9.6	306.7	2.3	2.3	446.3	132.9	5.9	2.63	1.58	1.24	SH
S27	9.6	9.2	-	-	-	-	-	-	-	-	-	SH
S28	9.6	9.7	355.0	0.8	0.2	174.1	0.1	5.5	0.33	1.31	-	I
S29	9.6	9.5	335.1	1.0	0.6	173.3	41.9	0.0	1.36	2.81	-	F

# test	d (mm)	L (mm)	UCS (MPa)	ϵ_{AMAX} (%)	X	ϵ'_A (s^{-1})	X	X	X	$E_{DISS-\sigma MAX}$ (MJ/m ³)	E_s (MJ/m ³)	damage
U1	21.0	20.6	245.3	0.5	-	6.7×10^6	-	-	-	0.84	-	sp + f
U2	20.8	20.5	203.0	0.4	-	6.7×10^6	-	-	-	0.55	-	sp
U3	20.9	19.9	273.1	0.3	-	6.7×10^6	-	-	-	0.54	-	sp
U4	20.9	20.7	206.7	0.3	-	6.7×10^6	-	-	-	0.47	0.47	sp + f
U6	20.9	20.7	217.3		gages broken	6.7×10^6	-	-	-	-	-	sp
U8	21.0	20.7	206.9		gages broken	6.7×10^6	-	-	-	-	-	sp
U9	24.4	59.9	229.7	-	-	6.7×10^5	-	-	-	-	-	sp
U10	24.4	57.7	224.1	0.3	-	6.7×10^5	-	-	-	0.36	-	sp
U11	24.8	54.8	294.6	0.5	-	6.7×10^5	-	-	-	0.61	-	sp
U12	24.3	41.7	-	-	-	6.7×10^5	-	-	-	-	-	f
U13	24.4	47.7	188.4	0.5	-	6.7×10^5	-	-	-	0.37	-	sp
U14	24.4	33.4	227.7	0.5	-	6.7×10^5	-	-	-	0.52	-	sp
U15	24.3	24.0	206.8	0.4	-	6.7×10^5	-	-	-	0.47	-	sp + f
U16	24.4	22.9	226.1	0.7	-	6.7×10^5	-	-	-	1.04	-	sp
U17	20.8	20.3	222.9	-	-	6.7×10^5	-	-	-	-	-	sp
U18	20.9	20.5	357.5	0.7	-	6.7×10^5	-	-	-	0.81	-	sp

Supplementary material for online publication only

[Click here to download Supplementary material for online publication only: Fondriest_et_al_suppl_mat_EPSL_revised.docx](#)

Supplementary material for online publication only

[Click here to download Supplementary material for online publication only: Fondriest_et_al_suppl_mat_EPSL_highlighted.docx](#)